COMPLIANCE CONTROL OF SHAD REDUNDANT ROBOT

A Thesis Submitted to the
Graduate School of Engineering and Sciences of
İzmir Institute of Technology
in Partial Fulfillment of the Requirements for the Degree of

MASTER OF SCIENCE

in Mechanical Engineering

by
Mert KANIK

December 2018
İZMİR

We approve the thesis of **Mert KANIK**

Examining Committee Members:

Assoc. Prof. Dr. M. İ. Can DEDE
Department of Mechanical Engineering, İzmir Institute of Technology

Prof. Dr. Serhan Özdemir
Department of Mechanical Engineering, İzmir Institute of Technology

Assist. Prof. Dr. Erkin GEZGİN
Department of Mechatronics Engineering, İzmir Katip Çelebi University

28 December 2018

Assoc. Prof. Dr. M. İ. Can DEDE
Supervisor
Department of Mechanical Engineering
İzmir Institute of Technology

Prof. Dr. Enver TATLICIOĞLU
Co-Supervisor
Department of Electrical & Electronics Engineering
İzmir Institute of Technology

Prof. Dr. Metin TANOĞLU
Head of the Department of
Mechanical Engineering

Prof. Dr. Aysun SOFUOĞLU
Dean of the Graduate School of
Engineering and Sciences

ABSTRACT

COMPLIANCE CONTROL OF SHAD REDUNDANT ROBOT

SHAD robot, which is located in IYTE Robotics Laboratory, is designed as a 4 degrees-of-freedom manipulator which has a PRRR serial kinematic structure. The prismatic joint works along the vertical axis, and the revolute joints rotate about the vertical axis. Although the positioning task on the plane can be executed by two revolute joints, SHAD robot is designed to be kinematically redundant using three revolute joints.

SHAD name is the abbreviations for SHoulder Haptic Device. The manipulator is constructed by using industrial servomotors coupled with high reduction ratio gears. Hence, this robot can only be used as a haptic device if admittance control is implemented for its control scheme. Accordingly, the aim of this study is to implement and test the admittance control algorithm on SHAD robot. However, since a human operator uses this haptic device when he/she is placed inside the workspace, certain safety precautions should be implemented. Therefore, initially, exploiting the kinematic redundancy of SHAD robot, an obstacle avoidance algorithm to move the robot's links away from the human operator is implemented and tested in simulations and experiments. To do this; (1) SHAD's mathematical model is derived, (2) This model is verified, and obstacle avoidance algorithm is validated by simulation tests in MATLAB/Simulink, (3) SHAD robot's experimental setup is developed, (4) Experimental tests for obstacle avoidance are conducted.

After the obstacle avoidance algorithm is implemented in the control of SHAD and proven that it works, admittance control experiments are carried out on human subjects to investigate the effects of the admittance term parameters, mass and damper, on certain performance metrics of the user. It is deduced that; (1) as the mass parameter of the admittance term is increased, accuracy of the operation is decreased while the total effort of the user is increased, (2) as the damper parameter of the admittance term is increased, both the accuracy of the operation and the total effort of the user are increased, (3) when the same corner frequency with different admittance term parameters are used, the accuracy of the operation is almost the same but total effort increases as the parameters increase.

ÖZET

ARTIKSIL SHAD ROBOTUNUN UYUMLULUK DENETİMİ

Bu tezde SHAD (SHoulder Haptic Device) olarak adlandırılan, IYTE robotik laboratuvarında konumlandırılan 4 serbestlik derecesine sahip PRRR türde seri bir robot kullanılmıştır. Kullanılan robotun prizmatik mafsalı robotun dikey yöndeki hareketini sağlarken, döner mafsallar ise robotun yataydaki hareketini sağlamaktadır. Düzlemde konumlama iki döner mafsal ile sağlanabilirken, SHAD üç döner mafsalı ile kinematik olarak artıksıl olarak tasarlanmıştır.

Robotta eklemlerdeki hareketin sağlanması için endüstriyel servo eyleyiciler ve bunlara bağlı yüksek çevrim oranlı dişli kutuları kullanılmıştır. Bundan dolayı, robotun haptik cihaz olarak kullanılabilmesi için admitans türünde bir kontrol uygulanması gerekmektedir. Buna bağlı olarak, tezin amacı admitans türünde bir kontrol algoritmasının SHAD'e uygulanması ve testlerinin gerçekleştirilmesidir. Robot haptik cihaz olarak kullanılırken, operatörün robotun çalışma uzayı içerisinde olduğundan, güvenlik önlemi uygulanmalıdır. Artıksıllıktan yararlanılan ve robotun uzuvlarının operatörden uzakta hareket etmesine dayalı oluşturulan engelden kaçınma algoritması, benzetim ortamında ve gerçek robot üzerinde uygulanmış ve testler gerçekleştirilmiştir. Bu amaçla izlenen yol şu şekildedir; SHAD'in matematiksel modelinin çıkartılması, çıkartılan modelinin doğrulanması ve oluşturulan engelden kaçınma algoritmasının MATLAB/Simulink ortamında benzetim testlerinin gerçekleştirilmesi, SHAD'in test kurulumunun oluşturulması ve engelden kaçınma algoritmasının gerçek robot üzerinde deneysel testlerinin gerçekleştirilmesidir.

Engelden kaçınmanın oluşturulmasından sonra, deneklerle admitans kontrol testlerine geçilmiş, testler sırasında elde edilen ölçümler aracılığıyla admitans terimi parametrelerinin (kütle ve damper) etkisi araştırılmıştır. Buradan çıkarılan sonuçlar şu şekilde olmuştur; kütle parametresi artırıldığında operasyonun hassasiyeti düşerken kullanıcının sağladığı toplam çaba artmaktadır, damper parametresi artırıldığında hem operasyonun hassasiyeti hem de kullanıcının sağladığı toplam çaba artmaktadır, aynı köşe frekansı ve farklı admitans terimi parametreleri kullanıldığında operasyonun doğruluğu hemen hemen aynı kalırken parametrelerin artışından kaynaklı toplam çaba artmaktadır.

TABLE OF CONTENTS

LIST OF FIGURES

LIST OF TABLES

Table **Page**

CHAPTER 1

INTRODUCTION

Robotic is an interdisciplinary branch of mechanical engineering, electrical engineering, computer science. Robotics field includes modeling, mechanical design, manufacturing, electromechanical design as well as designing control systems by making use of sensory feedback, information processing, and control theory. The field of robotics has been developed since the early 1960s with the design and control of general purpose robot manipulators. Since then, robotics found different areas of application different from assembly lines, particularly in the medical, defense, and service sectors, with the developments in both electromechanical systems and control systems. Since robots are started to be used in a variety of application areas and for different operations, new control strategies are devised in the literature and industry (Murray et al., 1994).

Especially in the industry, the robot controllers are generally utilized for tasks that includes the manipulation of mechanism that are composed of rigid bodies and joints in well-structured environments. These tasks generally require only motion trajectory tracking control of the of the robot's end-effector. However challenging problems with new application areas such as co-operative tasks with humans, extraterrestrial exploration and remote minimally invasive surgery, pave the way to higher performance and complicated control algorithms.

The other complicated tasks need control of physical contacts and mechanical interactions with the environment are material handling, assembling, painting, drilling. During the execution of these tasks, robots need to react to the forces applied to the its end-effector or comply with uncertainties of the environment. Control strategies such as compliance control can be used for executing these tasks. Compliance control lets robot to comply with interaction forces created by the contact with objects in the robot's environment or forces applied by a human during robot-human interaction (RHI) (Ahmet, 2011). Compliance control can be described as the control method that generates compliant motion. In 1987, Schutter defined compliant motion as "any robot motion during which the end-effector trajectory is modified, or even generated, based on online sensor information". In recent years, most of the researches in the compliance control is

related with the mechanical impedance of the robotic system, that is, the robot position or the dynamic relationship between velocity and external forces. In poorly configured environments, force feedback and force control are required for the robust and versatile behavior of the robotic system for safe and reliable operation especially for tasks carried out with humans.

Especially when RHI is considered, the field of haptics and haptic feedback are studied comprehensively in the literature. Haptic technology deals with the sense of touch and haptic interfaces are devices that enable a person to interact with a computer via physical sensations and movement. Haptic devices display the human a range of impedances that regulate the resistance that the human feels to his voluntary motion. Hence, the human feels the constrains that are generated in a virtual environment or sensed by a telerobot. Thereby, haptic interfaces allow a person to interact with a virtually created system, a distant environment via a slave manipulator or perform any task that requires RHI.

1.1 Aim of the study

In this study, the compliant control of the kinematically redundant SHAD (shoulder haptic device) robot located in Robotics Laboratory in İzmir Institute of Technology is accomplished. SHAD is a kinematically redundant robot, which is shown in Figure 1.1, one extra degree of freedom that can be used for obstacle avoidance subtask as mentioned in (Kanık et al., 2017). The robot was produced by Gökhan Berker during his Ph.D. studies in Izmir Institute of Technology to be used as a haptic device. The aim of this thesis is to integrate and test the proposed admittance controller alongside the obstacle avoidance subtask on SHAD robot. For these purposes, a mathematical model of the SHAD redundant robot is derived, and controller algorithms are devised for both motion trajectory tracking and compliant control with redundancy subtask.

Figure 1.1. The SHAD Robot

1.2 Outline

This thesis consists of 6 chapters which are Introduction, Literature Survey, Introduction to SHAD and Its Model, Experimental Setup, Control Algorithms and Tests, and Conclusions. In Chapter 2, an overview of haptics and haptic devices, comprehensive review on compliant control methods and a brief survey of kinematic redundancy in robot manipulators are presented. Later, in Chapter 3, SHAD redundant robot is introduced, and mathematical model of the robot is presented. Also, in Chapter 3, verification of dynamic model of SHAD is performed with simulations. Experimental setup, drive modes and homing procedure are explained in Chapter 4. Proposed control algorithms and the test results with these algorithms are explained in Chapter 5. Finally, in Chapter 6, a summary of the thesis and conclusions are given, and future works are discussed.

CHAPTER 2

LITERATURE SURVEY

Haptics term originates from Greek term “haptios” which describes sense of touch. This sense has a very important role in human perception alongside with the visual and auditory feedback. This sense helps humans to identify the limits of the human body which is used to sense distances and to calibrate the vision. When we touch a hot pan or hold a glass full of cold water, it allows us to distinguish between objects, feel if this physical interaction is harmful or not, and therefore sense of touch has preventive measures (Kern., 2009). The two structures for the haptic sense in our body are called tactile and kinesthetic perception. First one is tactile perception, which is the touch sensation provided by the nerve endings beneath our skin. The touch sensation provides us texture, temperature, and pressure information (Varalakshmi., 2012). On the other hand, kinesthetic perception provides information about motion, weight, and stiffness (Bilgincan et al., 2010).

2.1 Haptic Devices

In human-robot interaction, firstly visual and auditory senses were used. With the technological advances in data processing, haptic senses are begun to be used in human-robot interactions (Bilgincan et al., 2010). In terms of haptic information exchange, human-robot interactions are performed with haptic devices. Haptic devices let human to contact, sense and manipulate objects in virtual environments or distant environment by providing the necessary feedback about sense of touch (Hirche & Buss., 2012).

In haptic applications, the physical connection with the human transfers the mechanical resistance of the remote environment to the user and the mechanical resistance is called impedance. Mechanical impedance, Z_m, is the relationship between velocity, V and force, F;

$$Z_m = \frac{F}{V} \tag{2.1}$$

In Lawrence’s study (1993), Lawrence defined the transparency, T, is a factor that relates input impedance Z_{in} and output impedance of device Z_{out};

$$T = \frac{Z_{in}}{Z_{out}} \tag{2.2}$$

As transparency, T converges to "one" the output impedance gets closer to the input impedance, which means that user feels the desired impedance in an accurate way (Kern., 2009).

In Colgate and Brown's study (1994), Z_{width} is described as difference between the maximum impedance and minimum impedance. Z_{max} stands for the maximum impedance and Z_{min} stands for the minimum impedance that a haptic device can perform. Z_{width} can be thought as measure of quality of haptic device. As Z_{width} gets bigger, the dynamic range of passive impedances that can be rendered by a haptic display increase;

$$Z_{width} = \mathrm{Z_{max}} - \mathrm{Z_{min}} \tag{2.3}$$

Transparency and Z_{width} are used to describe the performance of the system in haptic systems. Z_{width} and transparency are related to sampling time of the controller, haptic device's friction, inertia, stiffness and backlash (Koul et al., 2013) (Lee et al., 2010).

Haptic devices are categorized as "impedance type" and "admittance type" devices. Impedance type devices measure the end-effector motion and generate output as force and/or torque. On the other hand, admittance type devices measure the force or torque between the device and the human and generate output as motion. In the next sections, admittance control is deeply investigated and reviewed in more detail since the haptic device in this thesis is admittance type haptic device.

2.1.1. Impedance Type Haptic Devices

For impedance type devices, the motion demands are transmitted from the user by using sensors such as encoders. On the other hand, commands from the controllers, the necessary force is transmitted to the user with the haptic interface's actuators. When impedance type haptic device is used by the human operator, operator always feels the inertia and friction of the manipulator during free motion. In case of designing an impedance type haptic device, it is required that the device's links have a sufficiently low inertia, low friction, and thus, high backdrivability. In this case, the user feels minimum level inertia of the links when passively backdriving the device (Herstenstein., 2011). Thus, this type devices are generally designed as lightweight, without backlash and with low mass properties (Adams and Hannaford., 2001).

Some of the commercially available desktop haptic devices are shown in Figure 2.1. Phantom Omni and Desktop devices are 6-DoF serial mechanisms with 3 passive orientational DoF. Falcon has a parallel structure with 3-DoF which allows to reflect forces in translational direction. On the other hand, SPIDAR is a cable driven 6 DoF haptic device. Table 2.1 shows the dimensions of the haptic devices shown in Figure 2.1.

Figure 2.1. Haptic interface devices
(Source:Tatematsu & Ishibashi., 2010)

Table 2.1. Haptic Interface Device Dimensions
(Source:Tatematsu & Ishibashi., 2010)

Device Name	Width (mm)	Height (mm)	Depth (mm)
Omni	160	120	70
Desktop	160	120	120
SPIDAR	200	120	200
Falcon	75	75	75

2.1.2. Admittance Type Haptic Devices

Admittance type devices are rarely used compared to impedance type devices. In haptic applications which have relatively larger size with respect to desktop devices, link masses and inertias increases. Also, gears used with high gear ratio lowers the

backdrivability of the device. In this case, the increased inertia of the links are felt by the user while passively backdriving the device. This increases the minimum impedance that can be reflected to the user. However, in the admittance type haptic device structures, the instantaneous forces applied by the user to the device are measured using a force / moment sensors. If the user pushes the device backwards, the backdriving is done by the controlling the actuators to move the manipulator so that zero force is applied as a resistance to the user. In this type of procedure, the devices which cannot be backdriven passively because of high reduction ratio are backdriven actively. Thus, in haptic applications that require large work space, even with high inertia of the links, admittance type haptic device can be used for active backdrivability.

The HapticMaster is a commercially available 3 DoF admittance type haptic device (initially built by FCS Control Systems) which is shown in Figure 2.2. Device has a force sensor located in the end-effector. The sensor is used for measuring human-machine interaction forces. This haptic device has 80.10^{-3} [m^3] workspace (Linde et al.,2002).

Figure 2.2. The HapticMaster
(Source: Linde et al., 2002)

Virtual Scenario Haptic Rendering Device (VISARD7) is another admittance type haptic device with 7 DoF. The link lengths are given in the Table 2.2. Device design guarantees that the end-effector of the device can move inside a half-cylinder with radius and height of 0.7 m. For force feedback control, the device has six-axis JR3 force-torque

sensor (Peer & Buss., 2008). The three dimensional computer aided design (3D-CAD) model of the device is shown in Figure 2.3.

Table 2.2. Link Lengths of VISARD7
(Source: Peer & Buss., 2008)

Link i	Length
l_1	0.6 m
$l_2=l_3$	0.36 m
$l_{4h}=l_6$	0.2155 m
l_{4v}	0.3411 m
l_5	0.082 m
l_7	0.0654 m

Figure 2.3. 3D-CAD model of VISARD7
(Source: Peer & Buss., 2008)

The specifications of the VISARD7 is given in Figure 2.4.

Property	Value
transl. workspace	$h = 0.6\,\mathrm{m}$ $d = 0.1\,\mathrm{m}$ $r_1 = 0.2\,\mathrm{m}$ $r_2 = 0.6\,\mathrm{m}$
rot. workspace*	pitch, roll: $\pm 360°$ yaw: $\pm 60°$
peak force	vertical: 533 N horizontal: 155 N
peak torque	pitch, yaw: 11 Nm roll: 4.8 Nm
trans. velocity	vertical: 0.895 m/s horizontal: 1.1 m/s
rot. velocity*	pitch, yaw: 4.3 rad/s roll: 8.9 rad/s
trans. acceleration	vertical: 9.2 $\mathrm{m/s^2}$ horizontal: 13.5 $\mathrm{m/s^2}$
rot. acceleration*	pitch, yaw: 183 $\mathrm{rad/s^2}$ roll: 318 $\mathrm{rad/s^2}$
maximum payload**	34 kg
mass of moving parts	$\approx$ 13 kg

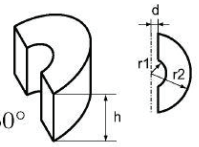

*numbers refer to a device controlled by inverse function, see Sec. IV-C1.
**calculated for zero steady-state human operator input force.

Figure 2.4. The Specifications of the VISARD7
(Source: Peer & Buss., 2008)

In this subsection, impedance and admittance type devices are briefly described. The structures of the devices are mentioned and compared. Due to their link size and backdrivability, the smaller devices are more suitable to be built as impedance type devices. In contrast to this, devices that have larger links, high gear ratios in their actuators are generally configured as admittance type devices with force and/or torque sensors.

2.2. Compliant Control

Some processes such as assembling, polishing, deburring processes, and applications that include RHI require the regulation of the physical contact of the robot. For these applications that involve contact, there is always a risk that robot may harm itself or objects in its environments. For this reason, compliant motion is necessity to carry out these tasks. As mentioned in Chapter 1, compliant motion of robots can be described as modification end-effector trajectory of a robot manipulator with online sensor information during end-effector motion (Jin et al., 2008).

Compliance control can be classified according to the compatibility type. According to this criterion, two basic groups can be formed. These are passive compliance control and active compliance control as stated in Siciliano & Khatib study, (2008).

In passive compliance control, the trajectory of the end point of the robot is adjusted by the interaction forces. This adjustment takes place due to the inherent compliance of the robot. The compliance may depend on structure of links, servo, joints or end-effector. Since there is no need for force and torque sensors, the passive approach to interaction control is easy and inexpensive. The predefined trajectory is not changed during the process. Furthermore, the active repositioning is slower than the passive compliance mechanism's response. However, passive compliance in industrial applications leads to deficiencies. For this reason, a separate robot end-effector must be provided and placed for each task. This type of control can only get over with slight position and orientation changes of the programmed trajectory. Finally, since force measurement is not performed, it may not prevent the occurrence of high contact forces (Vukobratovic et al., 2007), and (Siciliano & Khatib., 2008).

In the case of active compliance control, the compliance of the robotic system is provided by a specially designed control system. For this approach, it is often necessary to measure contact force and moment. This force and moment are fed back to the controller and used. So, the desired trajectory of the robot end-effector can be changed or recreated online. Active interaction control is slower than passive interaction control. Also, it is more expensive than the passive control because it needs sensors (Siciliano & Khatib., 2008).

2.2.1. Stiffness Controller

The stiffness of the joints determines the stiffness of the end-effector. Regulating the stiffness of the joints allows to reach the desired robot end-effector stiffness. So, during the end-effector tracking its trajectory, the desired force can be performed to the environment. Stiffness controller uses zeroth order impedance term while correlating the position with performed force.

Principle of stiffness control is shown in Figure 2.5. In Figure 2.5, J is the Jacobian matrix, $\underline{X}$ and $\underline{\dot{X}}$ represent end-effector's position and velocity vectors, $\underline{\tau}$ represents torques of joints, X_E is the displacement of environment and $K_E, K_V, and\ K_P$ shows

stiffness of contacting items, velocity feedback gain and position feedback gain, respectively. K_{F1} is compliance matrix and its used for to implement stiffness control and modify position command.

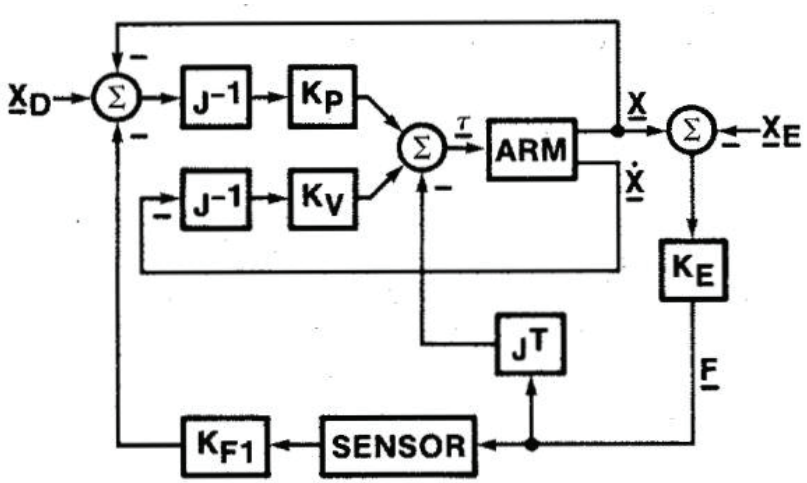

Figure 2.5. Stiffness control
(Source: Whitney., 1985)

The servo stiffness relies upon the feedback gain. Even though accurate position control requires high stiffness, for the force control, stiffness should be lower. According to this, servo's stiffness should be reduced. By reducing the stiffness, servo reduces the stiffness of the end-effector, resulting in better force control. (Dede., 2003)

2.2.2 Impedance Control

Another control strategy is impedance control. The aim of impedance control is to create relation between applied force and robots end-effector. As mentioned in section 2.1 mechanical impedance is Z_m. In frequency domain $F(s)$ is;

$$F(s) = Z_m(s)\dot{X}(s) \tag{2.4}$$

Second order impedance as;

$$sZ_m(s) = Ms^2 + Bs + K \tag{2.5}$$

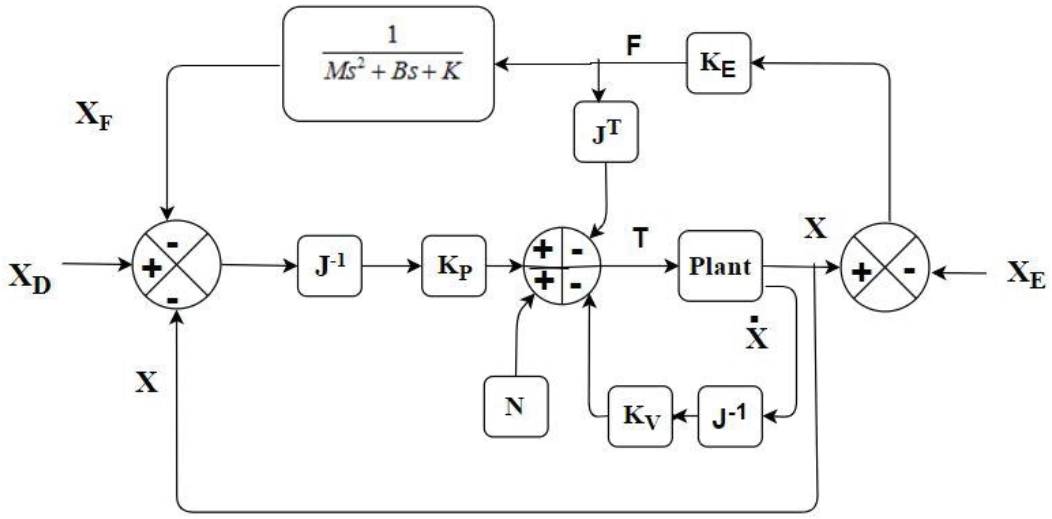

Figure 2.6. Impedance control
(Source: Işıtman., 2018)

Figure 2.6 shows basic impedance control. In the Figure 2.6, M, B, and K represents mass, damping and stiffness coefficients, respectively. According to this figure, desired impedance is a second order term. The term N is a feedforward control term that is used to cancel the nonlinear gravity, Coriolis and centrifugal effects.

In 1993, according to Volpe and Khosla, if the impedance controller is sensor based, it needs second order impedance term at most. This has two reasons, first reason is that second order systems are well studied and familiar, and second reason is the difficulty of obtaining measurements of higher order systems.

2.2.3 Hybrid Position / Force Control

Hybrid position / force control is another approach of compliant motion. Hybrid refers to merging force and position information in a control algorithm. The advantage of this control method over other control methods is that it evaluates force and position information separately. This separately processed information is evaluated separately in different control techniques and combined in the final stage (Dede., 2003).

In 1988, Anderson and Spong proposed hybrid position / force controller. Figure 2.7 shows the hybrid position / force control structure.

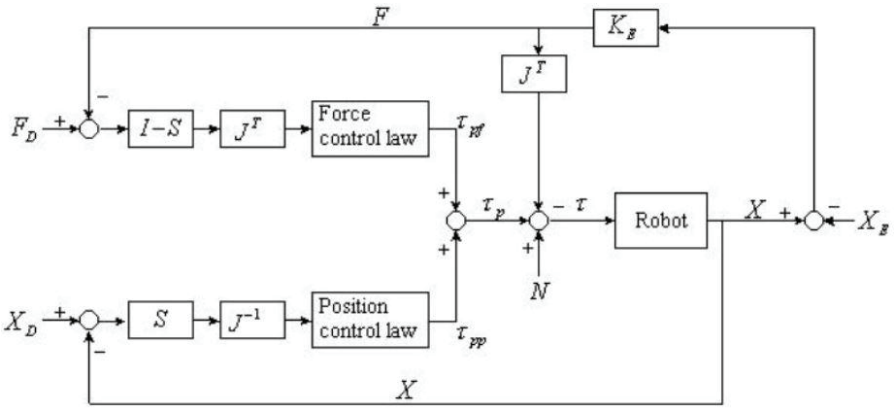

Figure 2.7. Hybrid position / force control
(Source: Anderson and Spong 1988)

In the Figure 2.7, S is compliance selection matrix and it can be constant, can vary by configuration or can continuously change with time. The subspaces of which position or which force should be controlled are determined by the S matrix (Fodor and Gabor., 1999).

2.2.4 Explicit and Implicit Force Control

Robot explicit force control consist of two categories. The first is force-based, and the second is position based force control (Zeng and Hemami., 1997). Figure 2.8 presents force based explicit controller. In this form of control, in order to obtain force error, directly measured force feedback is used. Force control law is defined to eliminate the error, and this is the concept of the controller. In the Figure 2.8, F_D, J^T, N, τ_p are desired force, Jacobian matrix, nonlinear terms and command torque, respectively.

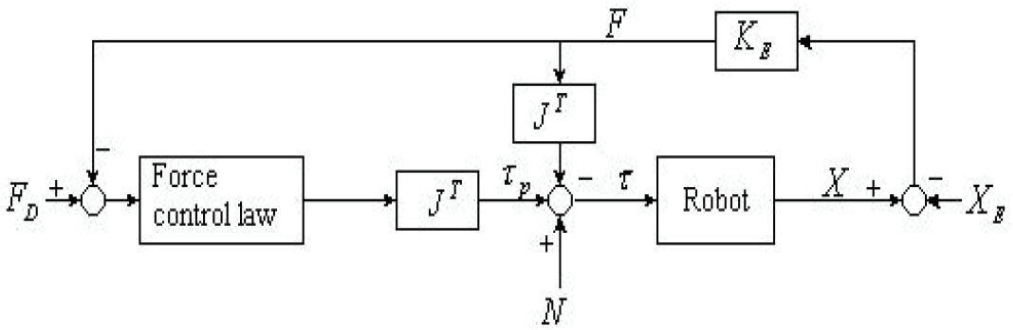

Figure 2.8. Explicit force control
(Source: Dede., 2003)

Figure 2.9 shows implicit force control. In this type, force feedback is not required and therefore no force sensor is required. The desired stiffness is used instead of force feedback. This is done by adjusting the gains of the servos, K_p, in the joints. The position is controlled according to the predefined position for a desired force (Whitney,1985).

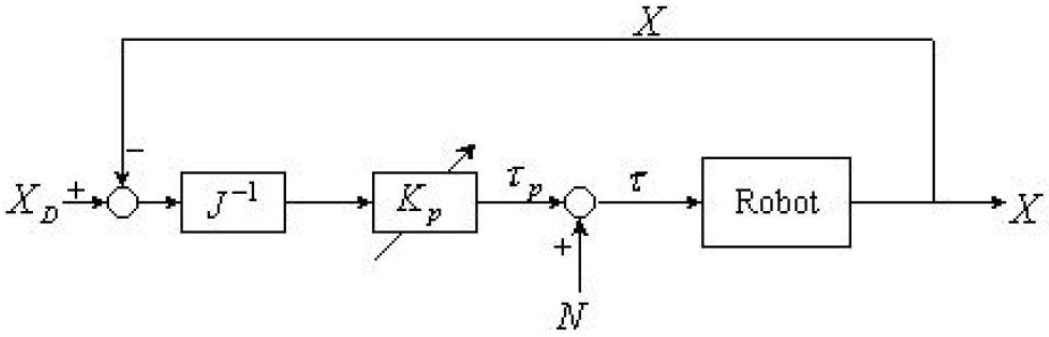

Figure 2.9. Implicit force control
(Source: Dede., 2003)

2.2.5. Admittance Control

Pure position control rejects the disturbance forces while executing the given reference motion trajectory. In contrast to pure position control, admittance control admits the disturbance forces. Admittance control type determines a force setpoint and this setpoint tracked by force compensator. The force compensator attempts to comply with the environmental interaction and react quickly to contact forces by rapidly modifying the reference motion trajectory (Seraji., 1994). The mechanical admittance, A defined as;

$$A = \frac{\dot{X}}{F} \tag{2.6}$$

Where, $\dot{X}$ is the end-effector velocity and F is the contact force. The size of admittance modifies the speed of motion according to applied force. Small admittance corresponds slow reaction while large admittance corresponds rapid reaction. If the compensator is defined in s domain;

$$X(s) = K(s)F(s) \tag{2.7}$$

$$K(s) = \frac{1}{s}A(s) \tag{2.8}$$

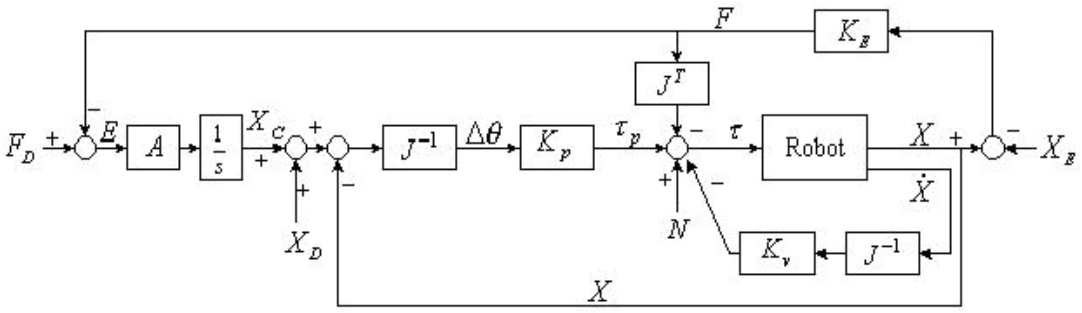

Figure 2.10. Admittance control
(Source: Dede., 2003)

Figure 2.10 shows scheme of common admittance control (Dede, 2003). A relates the force error vector E which is difference between desired force vector F_D with contact force vector F to the end-effector velocity perturbation. X_c defines command trajectory and equals;

$$X_c = \int A(F_d - F)dt \tag{2.9}$$

Choosing proper A can led to achieve effective and precise admittance control when the stiffness of environment is known. This admittance value varies according to various environments and may give sluggish results. For this reason, it is possible to change the admittance value by adaptive algorithms depending on the change in the environment. In Seraji study (1994), the control problem of manipulator which is under compliant motion when environment having an unknown stiffness is proposed. PID and PI force compensators are developed, and admittance control is used as explicit force control. The admittance, when the a second-order admittance is considered $A(s)$;

$$A(s) = k_d s^2 + k_p s + k_i \tag{2.10}$$

resulting in the PID force compensator;

$$K(s) = \frac{1}{s}A(s) = k_d s + k_p + \frac{k_i}{s} \tag{2.11}$$

The admittance, $A(s)$, when the a first-order admittance is considered, becomes;

$$A(s) = k_p s + k_i \tag{2.12}$$

resulting in the PI force compensator;

$$K(s) = \frac{1}{s}A(s) = k_p + \frac{k_i}{s} \tag{2.13}$$

In Saraji study, it is decided that, the adaptive admittance control studies which are proposed on their paper are useful for real-time force control (Seraji., 1994).

In 2010, Ott et al. proposed unified impedance and admittance control system approach. The control systems' stabilities and performances are complimentary. Ott et al. developed a system that both control systems are working together in a hybrid form. The algorithm lets the system switch between admittance and impedance control during operation. Performance of admittance and impedance controllers change depending on the stiffness of the environment. Figure 2.11 shows the performance of controllers against different environmental stiffness values.

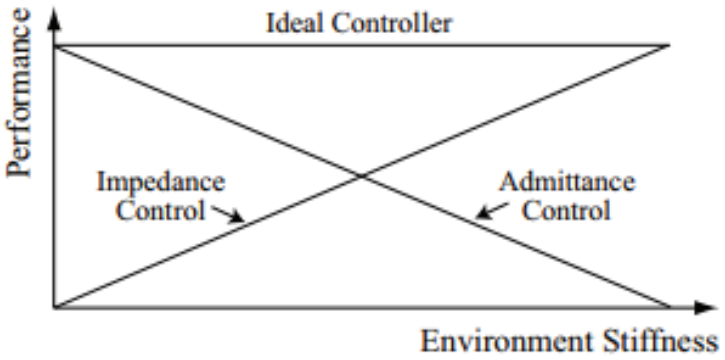

Figure 2.11. Admittance and impedance control for different environment stiffness (Source: Ott et al., 2010)

Admittance control provides good performance when the stiffness of environment is softer. But however, the performance of admittance control decreases as the stiffness of environment is gets larger. When stiffness of the environment is higher, impedance controller gives good performance but poor accuracy. Ott et al.'s approach claims that in one single framework, accuracy of admittance control and robustness properties of impedance control can be effectively combined (Ott et al., 2010).

Peer and Buss introduced a new admittance-type haptic interface for bimanual manipulation (2008). The system is composed of two 7 DoF admittance type haptic devices and mobile platform. Mobile platform provides large work space environment. This design concept decouples translational movement from rotational movements. Also, it helps to make simpler of control algorithms. Because of friction and the device dynamics, admittance control strategy is applied for VISARD7.

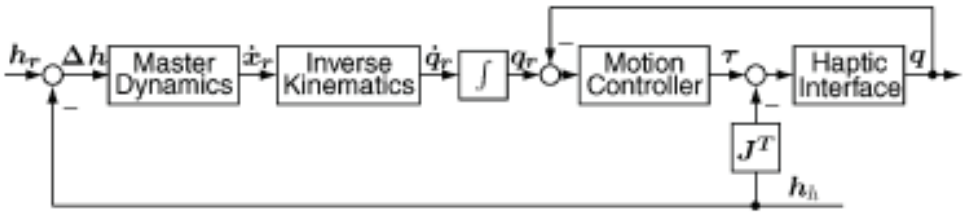

Figure 2.12. Admittance control scheme of VISARD7
(Source: Peer and Buss., 2008)

Figure 2.12 shows admittance control scheme which is applied for VISARD7. h_h describes force of human operator and measured by force sensor and h_r describes interaction force of telemanipulator with remote environment. Δh stands for substraction of h_h and h_r. Δh related by master dynamics to the refence end-effector velocity $\dot{x}_r$. Joint velocities $\dot{q}_r$ is calculated by inverse kinematics. Joint angles q_r are the reference inputs to a conventional position law. Two different motion controller approaches applied which are independent joint controller (IJCs) and a computed torque controller (CT) scheme (Khosla & Kanade., 1989). IJCs neglects the nonlinear behavior of the plant and cross couplings between the linkages so that CT scheme is used. The device performance is analyzed according to Cartesian position tracking performance.

In the study of Yu, Rosen and Li (2011), an exoskeleton system (EXO-UL7) is controlled. The control algorithm has two layers, lower level is controlled by using a PID controller. For the lower level, desired trajectories are generated by using 3 force sensors data in upper-level with admittance controller. Without model knowledge of exoskeleton device, designing a model-based impedance/admittance is not possible. For this reason, PID admittance control is chosen for upper level controller in order to regulate parameters with human impedance properties. Both control systems are used in task space.

2.3. Redundancy

Redundancy is proposed in many studies and the definitions are very close to each other. In 1997, Conkur and Buckingham clarified redundancy in robotics as: “The manipulator can be described as having n axes of motion and the space defined by the achievable motion of the end-effector will have a dimension m. The task space will give dimension r.”

- Case 1: $n = m$

This scenario is the standard for sufficient robot.

- Case 2: $n > m$

When n is chosen greater than m, the manipulator is redundant. In this situation configuration of the device can be change without changing end-effector pose.

- Case 3: $m > r$

In that case r is smaller than m and m is greater than n, this describes task redundancy.

These mathematical explanations can be transformed in to the following definitions:

- Definition 1: If the number of solutions to the inverse kinematics of a manipulator is not unique but finite, the manipulator is said to have multiple solutions.
- Definition 2: If the dimension of joint space is greater than the dimension of end-effector space then the device is kinematically redundant.
- Definition 3: If the task-space is completely contained by, and has a lower dimensionality than the end-effector space, the manipulator is said to be task redundant.

Redundancy can be used for a number of optimization cases including singularity avoidance (Yoshikawa., 1984), joint velocity minimization (Seraji., 1991), joint limit avoidance (Tatlicioğlu et al., 2005) and maximizing manipulability (Maaroof., 2012). Thus, redundancy increases dexterity.

For planar manipulators two DoF is enough for achieving positioning on plane. In this thesis work, SHAD has three DoF on plane. Thus, SHAD can be considered as a redundant robot. In this thesis, redundancy is being used for obstacle avoidance. Obstacle avoidance is used in cases where there are obstacles in the workspace of manipulator which may harm the environment or robot. It is especially important for operation when human compliance is involved. In case of redundancy the obstacle avoidance algorithms are adapted making use of self-motion of redundant robot. In our study robot and human interaction is exists and human operator is in work space of robot. Thus, the operator can be thought of as an obstacle to be avoided during operation. Therefore, obstacle avoidance as subtask is a suitable choice for this study.

Madani et al (2013) proposed adaptive variable structure controller for redundant manipulators which has a moving obstacle in manipulator's work space. For this controller there is no need for model. Manipulator's structure is enough for the control.

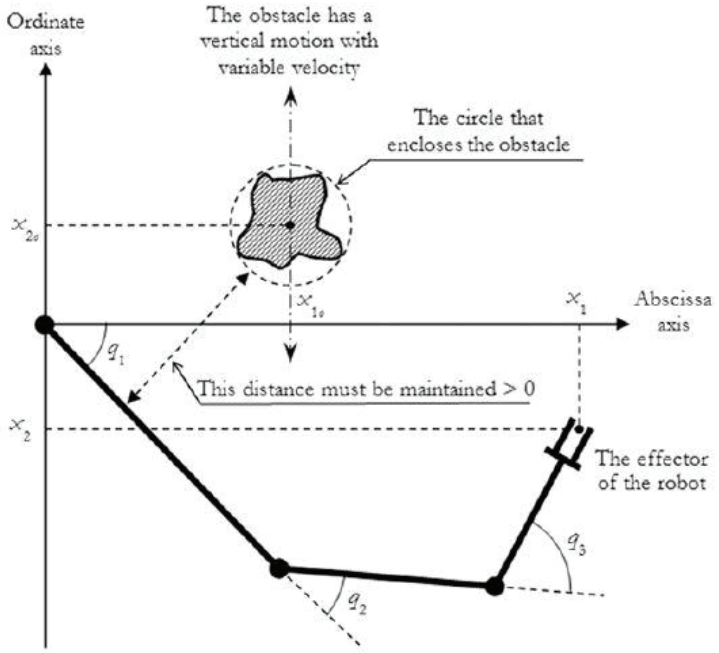

Figure 2.13. 3DoF redundant robot with mobile obstacle
(Source: Madani et al., 2013)

Madani et al. tested the controller performance with 3 DoF manipulator and Figure 2.13 shows 3 DoF redundant robot with mobile obstacle. The scheme of controller used by Madani et al. is shown in Figure 2.14.

In Figure 2.14, e represents tracking error,

$$e = x_m - x_s \tag{2.14}$$

X_0 is the position of obstacle, u is the joint torques, J is the Jacobian matrix, K_1, K_2, K_3, K_4 are variable terms, q is the joint positions, x is the end-effector position, r is the reference trajectory, and u^*;

$$u^* = K_1 + K_2 x_s + K_3 e + K_4 r \tag{2.15}$$

The controller pushes the model states of the manipulator to follow chosen reference model. 3 DoF redundant manipulator avoids obstacle during trajectory tracking.

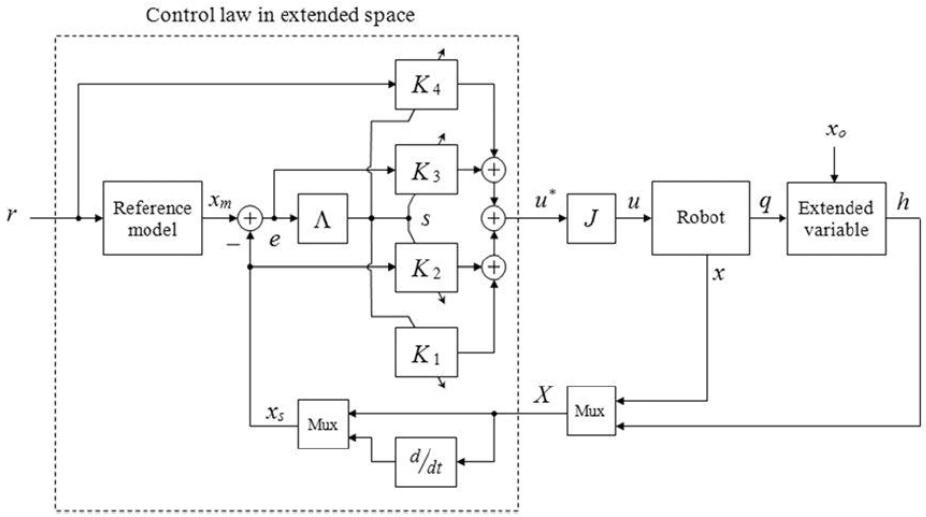

Figure 2.14. Variable structure controller
(Source: Madani et al., 2013)

In Maciejewski and Klein's study (1985), obstacle avoidance for kinematically redundant manipulator is handled. Their approach is to determine the required joint angle values for the manipulator under task with obstacle. The primary aim is to track end-effector trajectory. The secondary aim is to maximize the distance between the obstacles and links. Their formulation illustrated an extension to uses of the homogenous solution to include criteria that is better described in Cartesian world space coordinates.

In Lee and Buss's study (2007), several shortcomings are discussed when multiple obstacles are applied to avoid collision. They propose an unusual method of collision avoidance based on Jacobian transpose. In despite this, an efficient collision detection algorithm is presented. They show, if the minimum distance is formulated as an objective function, it would fail in some specific configuration, if the nearest distance is used it may cause chattering problem. As a solution for these problems, computationally simple method utilizing Jacobian transpose inverse kinematic is proposed.

In Zlajpah and Nemec's study (2002), they represent kinematic control algorithm for redundant manipulator with avoiding obstacle which moves in unstructured area. They use the internal motion of the manipulator for obstacle avoidance and their first aim is to follow desired trajectory for end-effector. Their approach is based on the redundancy resolution at the velocity level. They apply their algorithm to highly redundant manipulator and illustrate in an unstructured and time-varying environment. Also, they

test the algorithm with a four-link planar manipulator and simple vision system to detect obstacle. The test results verify that the proposed algorithm is suitable for real-time control.

2.4. Conclusion

In this section, firstly literature survey for haptics and haptic devices are presented. Examples of devices with haptic structure are given and working principles are mentioned.

Secondly, the compliance control is explained. Information about the control algorithms covered by compliance controls are given. In addition, working principles of these control algorithms are mentioned.

After that, kinematic redundancy is explained, and application methods of kinematic redundancy are mentioned. In addition, the reason for using the obstacle avoidance algorithm as subtask is explained. Lastly, studies on the obstacle avoidance algorithms in the literature are mentioned.

CHAPTER 3

INTRODUCTION TO SHAD ROBOT AND ITS MODEL

SHAD robot system is a 4-DoF robot arm with a prismatic joint and three revolute joint, which have parallel axes of rotation. Its dimensions are selected to have a workspace that can cover the whole arm motion of a human in standing and sitting positions. SHAD robot system's setup consists of SHAD manipulator and its control panel. SHAD and its joint locations are shown in Figure 3.1.

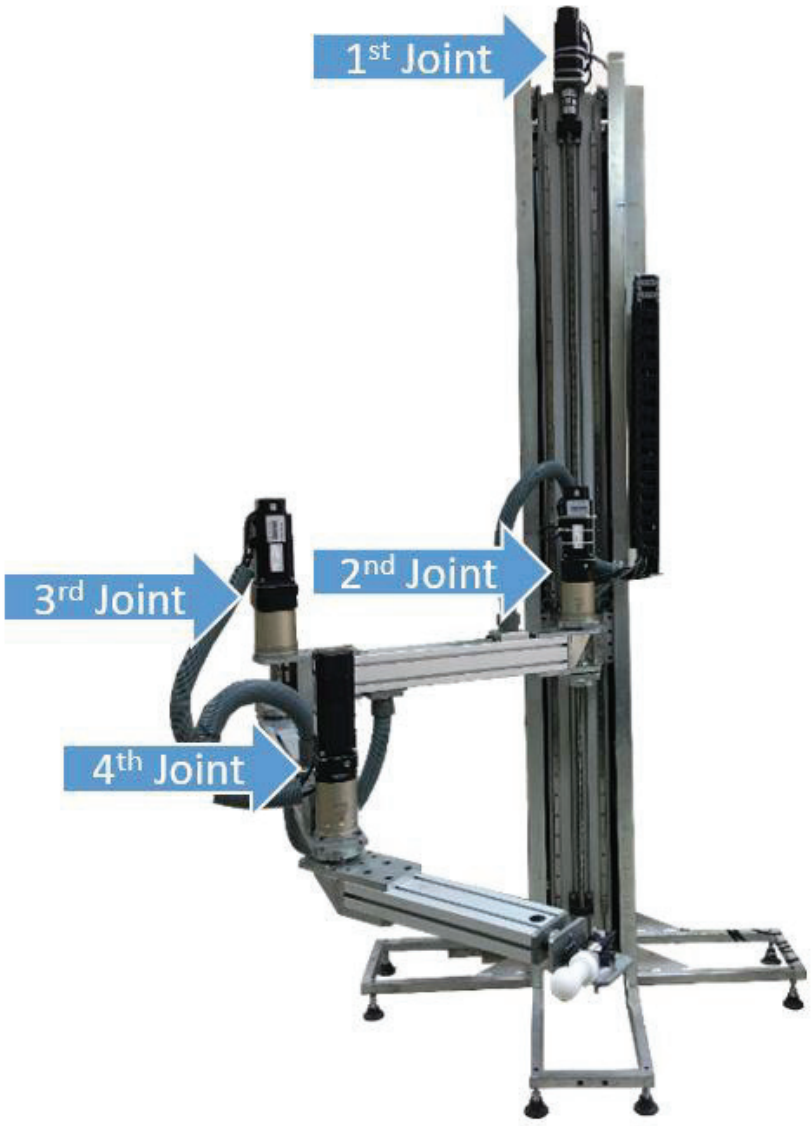

Figure 3.1. SHAD and its joints

The characteristics of the actuators used on the joints, the encoders used as angular position sensor attached to the rear end of the actuators and the gearboxes are listed in Table 3.1 and shown in Figure 3.2. The brand of the actuators, drivers and encoders are LS Mecapion. There are only 3 gearboxes used in the robot system. Except the first link, every actuator has a gearbox mounted at their output shafts and their reduction ratios are 1:70. Planetary gear reduction system are used as the gearbox. The motion of the device along the prismatic axis is provided by slideways and ball screw which is coupled to another LS Mecapion actuator. The pitch value of the ball screw is 10 mm/rev. In addition, a counter mass (50 kg) is used for gravity compensation.

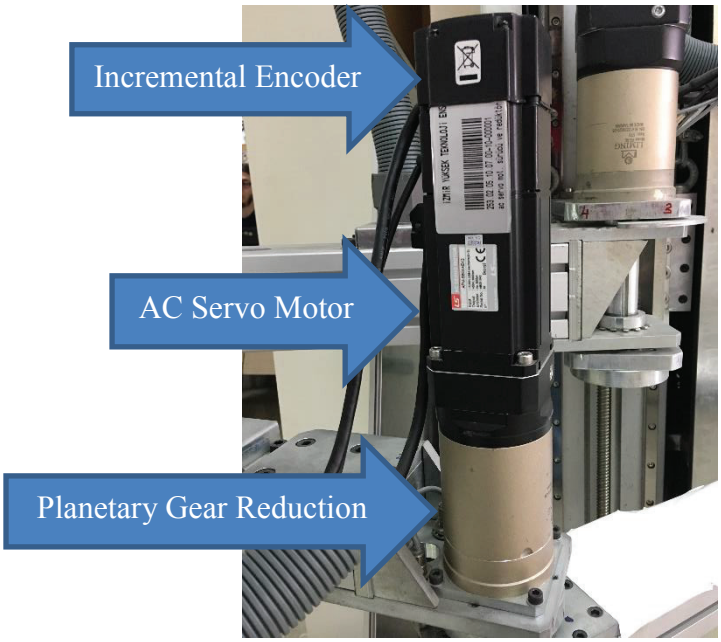

Figure 3.2. SHAD actuator components

Table 3.1. Models, encoder types and reduction ratios of actuators

Joint Number	Motor Code	Motor Power (W)	Encoder Type	Reduction Ratio	Reduction Type
1	APM-SC08	800	Incremental	No Reduction	No Reductiom
2	APM-SC08	800	Incremental	1:70	Planetary Gear
3	APM-SC08	800	Incremental	1:70	Planetary Gear
4	APM-SC04	400	Incremental	1:70	Planetary Gear

Besides the kinematic structure, the control panel of the system consists of 5 drivers and 6 electrical terminals for transmitting and receiving signals in between a data acquisition (DAQ) system and drivers. A data acquisition system is required to feed the inputs to the joint actuator in real-time while acquiring the sensory information from the actuator drivers. In this way, SHAD's control algorithm can be implemented on a host PC containing this DAQ system. Figure 3.3 shows control panel and the connection details inside the control panel are presented in Appendix A. 4 of the 5 drivers that are observed in Figure 3.3 are used for SHAD and the last one is used for an extra single DoF system outside the SHAD robot. Drivers are LS Mecapion drivers and their model are VS04G4N-P1. Actuators have an electromechanical brake and incremental quadrature encoders with 3000 pulses per revolution (ppr) are coupled to the rear end of these actuators.

Figure 3.3. SHAD control panel

3.1 Kinematic Analysis of SHAD

SHAD robot is a 4-DoF haptic device. The device consists of a prismatic joint, and three revolute joints. Axes of the all joints are parallel to each other (Z_1, Z_2, Z_3, Z_4). The prismatic joint on the device is intended to move the plane of the revolute joints up and down. The movement of the device in the x-y plane is provided by revolute joints that is presented by a basic sketch of the manipulator which is shown in Figure 3.4. With respect to this sketch, the link length a_1 can be taken as zero and the location of the base frame denoted with x-y-z in Figure 3.4 can be moved by a_1 distance along the x-axis. Therefore, a_1 link length is not considered in mathematical model. The other effective link lengths are represented by a_2, a_3, and a_4. Masses of the links are represented by m_1, m_2, m_3 and m_4. l_2, l_3, l_4 are the distances between joints and centre of mass of links.

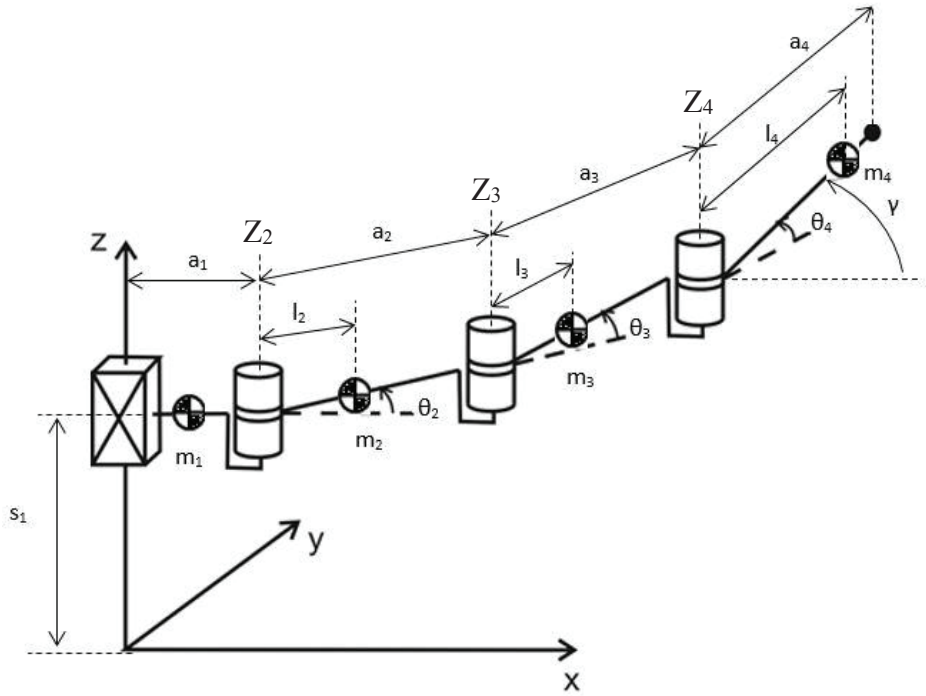

Figure 3.4. Kinematic sketch of SHAD

3.1.1. Forward Kinematics

Forward kinematics analysis is a necessity to map the joint motions to the end-effector motions. Using the link parameters expressed in Figure 3.4, forward kinematics equations are formulated as shown in Equation.3.1.

$$
\begin{aligned}
\theta_{23} &= \theta_2 + \theta_3 \\
\theta_{234} &= \theta_2 + \theta_3 + \theta_4 \\
x &= a_2 cos\theta_2 + a_3 cos\theta_{23} + a_4 cos\theta_{234} \\
y &= a_2 sin\theta_2 + a_3 sin\theta_{23} + a_4 sin\theta_{234} \\
z &= s_1 \\
\gamma &= \theta_2 + \theta_3 + \theta_4
\end{aligned}
\tag{3.1}
$$

Velocity equations for forward kinematic analysis are derived by differentiating the position level equation in Equating 3.1. with respect to time as shown in Equation 3.2.

$$
\begin{aligned}
\dot{x} = (&-a_2 sin\theta_2 - a_3 sin\theta_{23} - a_4 sin\theta_{234})\dot{\theta}_2 \\
&+ (-a_3 sin\theta_{23} - a_4 sin\theta_{234})\dot{\theta}_3 \\
&+ (-a_4 sin\theta_{234})\dot{\theta}_4 \\
\dot{y} = (&a_2 cos\theta_2 + a_3 cos\theta_{23} + a_4 cos\theta_{234})\dot{\theta}_2 \\
&+ (a_3 cos\theta_{23} + a_4 cos\theta_{234})\dot{\theta}_3 \\
&+ (a_4 cos\theta_{234})\dot{\theta}_4 \\
\dot{z} &= \dot{s}_1 \\
\dot{\gamma} &= \dot{\theta}_2 + \dot{\theta}_3 + \dot{\theta}_4
\end{aligned}
\tag{3.2}
$$

Equation 3.2. can be reorganized in matrix form as follows;

$$
\begin{bmatrix} \dot{x} \\ \dot{y} \\ \dot{z} \\ \dot{\gamma} \end{bmatrix} = \hat{J} \begin{bmatrix} \dot{s}_1 \\ \dot{\theta}_2 \\ \dot{\theta}_3 \\ \dot{\theta}_4 \end{bmatrix} \tag{3.3}
$$

Jacobian matrix, $\hat{J}$, can thus be written for the sufficient manipulator configuration as shown in Equation 3.4.

$$
\hat{J} = \begin{bmatrix} 0 & -a_2 sin\theta_2 - a_3 sin\theta_{23} - a_4 sin\theta_{234} & -a_3 sin\theta_{23} - a_4 sin\theta_{234} & -a_4 sin\theta_{234} \\ 0 & a_2 cos\theta_2 + a_3 cos\theta_{23} + a_4 cos\theta_{234} & a_3 cos\theta_{23} + a_4 cos\theta_{234} & a_4 cos\theta_{234} \\ 1 & 0 & 0 & 0 \\ 0 & 1 & 1 & 1 \end{bmatrix} \tag{3.4}
$$

Although the motion required for the positioning task in the x-y plane can be achieved by two revolute joints, the device is designed to be kinematically redundant using three revolute joints. In this way, extra tasks can be done such that the device can avoid obstacles that may be present during this planar motion. Actual link lengths of the manufactured device are shown in Table 3.2 and maximum achievable position of the prismatic joint s_1 is limited by 2000 mm with respect to robot's reference frame.

Table 3.2. Link lengths of device

Links	Link Lengths (mm)
a_2	800
a_3	700
a_4	500

3.1.2. Inverse Kinematics

For a specified end-effector position, positions of the joints can be found by inverse kinematics calculations. The first joint position is the position of the linear axis which is equal to the end-effector's position along z-axis in task space as shown in Equation 3.5.

$$s_1 = z \tag{3.5}$$

End-effector's position along x- and y-axes can be rewritten by using the specified end-effector orientation information, $\gamma = \theta_2 + \theta_3 + \theta_4$, as shown in Equation 3.6.

$$\begin{aligned} x &= a_2 cos\theta_2 + a_3 cos\theta_{23} + a_4 cos\gamma \\ y &= a_2 sin\theta_2 + a_3 sin\theta_{23} + a_4 sin\gamma \end{aligned} \tag{3.6}$$

Since the orientation of the end-effector in the inverse task is a given, all the known parts of the equations in Equation 3.6 are placed on the left side of the equality as presented in Equation 3.7.

$$\begin{aligned} x^* &= x - a_4 cos\gamma = a_2 cos\theta_2 + a_3 cos\theta_{23} \\ y^* &= y - a_4 sin\gamma = a_2 sin\theta_2 + a_3 sin\theta_{23} \end{aligned} \tag{3.7}$$

When the two equations presented in Equation 3.7 are squared and summed, by using trigonometric equalities the following equation is formed;

$$x^{*^2} + y^{*^2} = a_2^2 + a_3^2 + 2a_2 a_3 cos\theta_3 \tag{3.8}$$

Angular position of the third joint, θ_3, is calculated from Equation 3.8 as;

$$\begin{aligned} cos\theta_3 &= \frac{x^{*^2} + y^{*^2} - a_2^2 - a_3^2}{2a_2 a_3} \\ sin\theta_3 &= \sigma_3 \sqrt{1 - cos^2\theta_3} \qquad \sigma_3 = \pm 1 \\ \theta_3 &= atan_2(\sigma_3 \sqrt{1 - cos^2\theta_3}, cos\theta_3) \end{aligned} \tag{3.9}$$

When trigonometric equalities for $cos\theta_{23}$ and $sin\theta_{23}$ functions are implemented to write them in their open forms, equations in Equation 3.7 is rewritten as shown in Equation 3.10.

$$\begin{aligned} x^* &= a_2 cos\theta_2 + a_3(cos\theta_2 cos\theta_3 - sin\theta_2 sin\theta_3) \\ &= (a_2 + a_3 cos\theta_3)cos\theta_2 - a_3 sin\theta_3 sin\theta_2 \\ y^* &= a_2 sin\theta_2 + a_3(cos\theta_2 sin\theta_3 + cos\theta_3 sin\theta_2) \\ &= (a_3 sin\theta_3)cos\theta_2 + (a_2 + a_3 cos\theta_3)cos\theta_2 \end{aligned} \tag{3.10}$$

When Equation 3.10 is reorganized in matrix form;

$$\begin{bmatrix} a_2 + a_3 cos\theta_3 & -a_3 sin\theta_3 \\ a_3 sin\theta_3 & a_2 + a_3 cos\theta_3 \end{bmatrix} \begin{bmatrix} cos\theta_2 \\ sin\theta_2 \end{bmatrix} = \begin{bmatrix} x^* \\ y^* \end{bmatrix} \tag{3.11}$$

Then the angular position of the second joint, θ_2, is calculated as shown below:

$$\begin{aligned} sin\theta_2 &= \frac{y^*(a_2 + a_3 cos\theta_3) - x^*(a_3 sin\theta_3)}{a_2^2 + a_3^2 + 2a_2 a_3 cos\theta_3} \\ cos\theta_2 &= \frac{x^*(a_2 + a_3 cos\theta_3) + y^*(a_3 sin\theta_3)}{a_2^2 + a_3^2 + 2a_2 a_3 cos\theta_3} \\ \theta_2 &= atan_2(sin\theta_2, cos\theta_2) \end{aligned} \tag{3.12}$$

Finally, the angular position of the fourth joint, θ_4, is calculated as shown in Equation 3.13.

$$\theta_4 = \gamma - \theta_3 - \theta_2 \tag{3.13}$$

Until this point, inverse kinematic equations are derived for a sufficient manipulator operation where the task space translational positions and velocities are defined along with the orientation and angular velocity of the end-effector about the z-axis. However, it is aimed for SHAD to operate as a redundant manipulator where only the translational velocities of the end-effector are specified. In this case, in velocity level inverse kinematics calculations, there will be four unknowns (joint velocities) and three equations for given end-effector's translational velocities. This results in infinite number of solutions, thus gives us the opportunity for optimization by implementing secondary tasks.

Jacobian matrix is re-written for the redundant configuration as;

$$\hat{J}_r = \begin{bmatrix} 0 & -a_2 sin\theta_2 - a_3 sin\theta_{23} - a_4 sin\theta_{234} & -a_3 sin\theta_{23} - a_4 sin\theta_{234} & -a_4 sin\theta_{234} \\ 0 & a_2 cos\theta_2 + a_3 cos\theta_{23} + a_4 cos\theta_{234} & a_3 cos\theta_{23} + a_4 cos\theta_{234} & a_4 cos\theta_{234} \\ 1 & 0 & 0 & 0 \end{bmatrix} \tag{3.14}$$

where the vector of the joint velocities stayed the same but the composition and size of the task space velocities have changed and presented below.

$$\bar{\omega} = \begin{bmatrix} \dot{s}_1 \\ \dot{\theta}_2 \\ \dot{\theta}_3 \\ \dot{\theta}_4 \end{bmatrix} \tag{3.15}$$

$$\bar{V} = \begin{bmatrix} \dot{x} \\ \dot{y} \\ \dot{z} \end{bmatrix} \tag{3.16}$$

$$\bar{\omega} = \hat{J}^* \bar{V} \tag{3.17}$$

As a result, making use of minimum norm of joint motion criteria, the pseudo-inverse is defined as;

$$\hat{J}^* = \hat{J}_r^T \left(\hat{J}_r \hat{J}_r^T \right)^{-1} \tag{3.18}$$

However, the solution using the pseudo inverse is not unique and can be further used for optimization. The optimization for obstacle avoidance is discussed in Chapter 5.

3.2 Dynamic Model of SHAD

In haptic systems to simulate virtual wall information or collisions, forces displayed at the end-effector are used. Therefore, quasi-static force analysis is required to calculate the amount of force/torques to be supplied by each joint of SHAD to display the demanded force at the handle of the device. In quasi-static force analysis, motion in terms of acceleration and velocities are assumed to be zero and since the gravity is compensated by a counter-mass in SHAD, gravitational forces are neglected. Making use of virtual work principle, the formulation to calculate the force/torques of joints for applying demanded forces at the tip point is presented in Equation 3.19.

$$\bar{\tau}_q = -\hat{J}_r^T \bar{F} \tag{3.19}$$

Where $\bar{\tau}_q$ defines the joint force/torque vector,

$$\bar{\tau}_q = \begin{bmatrix} F_{q1} \\ \tau_{q2} \\ \tau_{q3} \\ \tau_{q4} \end{bmatrix} \tag{3.20}$$

And $\bar{F}$ defines the force vector to be displayed to the operator through the handle in task space coordinate system.

$$\bar{F} = \begin{bmatrix} F_x \\ F_y \\ F_z \end{bmatrix} \tag{3.21}$$

Forward dynamic analysis of the manipulator is carried out by using the Euler-Lagrangian equations. The Lagrangian term, L, is defined as kinetic energy, KE, minus the potential energy, PE. However, in SHAD, the use of counter-mass, $\mathrm{m_b} = \mathrm{m_1} + \mathrm{m_2} + \mathrm{m_3} + \mathrm{m_4}$, cancels the effect of potential energy and makes the change in potential energy equal to zero. Therefore, the Lagrangian term, L, is equal to the kinetic energy, KE. In Equation 3.22, KE is substituted for L.

$$\frac{d}{dt}\left(\frac{\partial KE}{\partial \dot{q}_k}\right) - \frac{\partial KE}{\partial q_k} = Q_k \tag{3.22}$$

In Equation 3.22, Q_k is the force/torque applied by the k[th] joint, q_k is the k[th] joint variable and $\dot{\mathrm{q}}_\mathrm{k}$ is the time derivative of the k[th] joint variable. Kinetic Energy equation for the whole arm is presented in Equation 3.23.

$$\begin{aligned} KE = \frac{1}{2}m_1 v_1^2 + \frac{1}{2}m_2 v_2^2 + \frac{1}{2}m_3 v_3^2 + \frac{1}{2}m_4 v_4^2 + \frac{1}{2}I_2\omega_2^2 \\ + \frac{1}{2}I_3\omega_3^2 + \frac{1}{2}I_4\omega_4^2 \end{aligned} \tag{3.23}$$

Mass centre velocity calculations are indicated in Equation 3.24, 3.25, 3.26 and 3.27.

$$\begin{aligned} v_1 &= \dot{s}_1 \\ v_1^2 &= \dot{s}_1^2 \end{aligned} \tag{3.24}$$

$$\begin{aligned} P_{m_2} &= l_2 cos\theta_2\, \vec{\imath} + l_2 sin\theta_2 \vec{\jmath} + s_1\vec{k} \\ v_2^2 &= \frac{dP_{m_2}}{dt} = \dot{s}_1^2 + l_2^2\dot{\theta}_2^2 \\ \omega_2^2 &= \dot{\theta}_2^2 \end{aligned} \tag{3.25}$$

$$\begin{aligned} P_{m_3} &= (a_2 cos\theta_2 + l_3 cos\theta_{23})\vec{\imath} + (a_2 sin\theta_2 + l_3 sin\theta_{23})\vec{\jmath} \\ &\quad + s_1\vec{k} \\ v_3 &= \frac{dP_{m_3}}{dt} \\ \omega_3^2 &= \dot{\theta}_2^2 + \dot{\theta}_3^2 + 2\dot{\theta}_2\dot{\theta}_3 \end{aligned} \tag{3.26}$$

$$\begin{aligned} P_{m_4} &= (a_2 cos\theta_2 + a_3 cos\theta_{23} + l_4 cos\theta_{234})\vec{\imath} \\ &\quad + (a_2 sin\theta_2 + a_3 sin\theta_{23} + l_4 sin\theta_{234})\vec{\jmath} + s_1\vec{k} \\ v_4 &= \frac{dP_{m_4}}{dt} \end{aligned} \tag{3.27}$$

$$
\begin{aligned}
v_4^2 = \dot{s}_1^2 + (a_2^2 + a_3^2 + l_4^2 + 2a_2a_3cos\theta_3 + 2a_2l_4cos\theta_{34} \\
+ 2a_3l_4cos\theta_{34})\dot{\theta}_2^2 \\
+ (a_3^2 + l_4^2 + 2a_3l_4cos\theta_4)\dot{\theta}_3^2 + (l_4^2)\dot{\theta}_4^2 \\
+ (2a_2a_3cos\theta_3 + 2a_2l_4cos\theta_{34} + 2a_3^2 \\
+ 4a_3l_4cos\theta_4 + 2l_4^2)\dot{\theta}_2\dot{\theta}_3 \\
+ (2a_2l_4cos\theta_{34} + 2a_3l_4cos\theta_4 + 2l_4^2)\dot{\theta}_2\dot{\theta}_4 \\
+ (2a_3l_4cos\theta_4 + 2l_4^2)\dot{\theta}_3\dot{\theta}_4 \\
\omega_4^2 = \dot{\theta}_2^2 + \dot{\theta}_3^2 + \dot{\theta}_3^2 + 2\dot{\theta}_2\dot{\theta}_3 + 2\dot{\theta}_2\dot{\theta}_4 + 2\dot{\theta}_3\dot{\theta}_4
\end{aligned}
$$

Substituting Equation 3.24, 3.25, 3.26 and 3.27, kinetic energy equation can be re-written as shown in Equation 3.28.

$$
\begin{aligned}
KE = \frac{1}{2}m_{11}\dot{s}_1^2 + \frac{1}{2}m_{22}\dot{\theta}_2^2 + \frac{1}{2}m_{33}\dot{\theta}_3^2 + \frac{1}{2}m_{44}\dot{\theta}_4^2 + m_{23}\dot{\theta}_2\dot{\theta}_3 \\
+ m_{24}\dot{\theta}_2\dot{\theta}_4 + m_{34}\dot{\theta}_3\dot{\theta}_4
\end{aligned} \tag{3.28}
$$

Where;

$$
\begin{aligned}
m_{11} = (m_1 + m_2 + m_3 + m_4) \\
m_{22} = m_2l_2^2 + m_3(a_2^2 + l_3^2 + 2a_2l_3cos\theta_3) \\
+ m_4(a_2^2 + a_3^2 + l_4^2 + 2a_2a_3cos\theta_3 \\
+ 2a_2l_4cos\theta_{34} + 2a_3l_4cos\theta_4) + I_2 + I_3 + I_4 \\
m_{23} = m_3(a_2l_3cos\theta_3 + l_3^2) + m_4(a_2a_3cos\theta_3 + a_2l_4cos\theta_{34} \\
+ a_3^2 + 2a_3l_4cos\theta_4 + l_4^2) + I_3 + I_4 \\
m_{24} = m_4(a_2l_4cos\theta_{34} + a_3l_4cos\theta_4 + l_4^2) + I_4 \\
m_{33} = m_3l_3^2 + m_4(a_3^2 + l_4^2 + 2a_3l_4cos\theta_4) + I_3 + I_4 \\
m_{34} = m_4(a_3l_4cos\theta_4 + l_4^2) + I_4 \\
m_{44} = m_4l_4^2 + I_4
\end{aligned} \tag{3.29}
$$

Dynamic equation using the Euler-Lagrangian formulation for SHAD is represented as shown in Equation 3.30.

$$
\sum_{j=1}^{4} m_{kj}\ddot{q}_j + \sum_{j=1}^{4} B_{kj}\dot{q}_j^2 + \sum_{j=1}^{3}\sum_{i=j+1}^{4} \gamma_{kji}\dot{q}_j\dot{q}_i + G_k = Q_k \tag{3.30}
$$

Since there is a counter mass, gravitational effects are neutralized, $G_k = 0$ for $k = 1, 2, 3, 4$. Centripetal force coefficients are calculated as;

$$
B_{kj} = \frac{\partial m_{kj}}{\partial q_j} - \frac{1}{2}\frac{\partial m_{jj}}{\partial q_k} \tag{3.31}
$$

and Coriolis force coefficients are calculated as;

$$\gamma_{kji} = \frac{\partial m_{kj}}{\partial q_i} - \frac{\partial m_{ji}}{\partial q_k} + \frac{\partial m_{ik}}{\partial q_j} \tag{3.32}$$

- For the first DoF,

All B_{kj} and γ_{kji} are zero. So;

$$m_{12} = m_{13} = m_{14} = 0 \tag{3.33}$$

Finally, the dynamic equation of motion for the first joint is calculated with respect to the moving counter-mass and the arm mass as;

$$F_1 = (m_1 + m_2 + m_3 + m_4)\ddot{s}_1 \tag{3.34}$$

- For the second DoF,

$$B_{21} = B_{22} = 0 \tag{3.35}$$

$$\begin{aligned} B_{23} &= \frac{\partial m_{23}}{\partial \theta_3} - \frac{1}{2}\frac{\partial m_{33}}{\partial \theta_2} \\ &= -m_3 a_2 l_3 sin\theta_3 \\ &\quad - m_4(a_2 a_3 sin\theta_3 + a_2 l_4 sin\theta_{34}) \end{aligned} \tag{3.36}$$

$$B_{24} = \frac{\partial m_{24}}{\partial \theta_4} - \frac{1}{2}\frac{\partial m_{44}}{\partial \theta_2} = -m_4(a_2 l_4 sin\theta_{34} + a_3 l_4 sin\theta_4) \tag{3.37}$$

$$\gamma_{212} = \gamma_{213} = \gamma_{214} = 0 \tag{3.38}$$

$$\begin{aligned} \gamma_{223} &= \frac{\partial m_{22}}{\partial \theta_3} - \frac{\partial m_{23}}{\partial \theta_2} + \frac{\partial m_{23}}{\partial \theta_2} \\ &= -2m_3 a_2 l_3 sin\theta_3 - 2m_4 a_2 a_3 sin\theta_3 \\ &\quad - 2m_4 a_2 l_4 sin\theta_{34} \end{aligned} \tag{3.39}$$

$$\begin{aligned} \gamma_{224} &= \frac{\partial m_{22}}{\partial \theta_4} - \frac{\partial m_{24}}{\partial \theta_2} + \frac{\partial m_{24}}{\partial \theta_2} \\ &= -2m_4 a_2 l_4 sin\theta_{34} - 2m_4 a_3 l_4 sin\theta_4 \end{aligned} \tag{3.40}$$

$$\begin{aligned} \gamma_{234} &= \frac{\partial m_{23}}{\partial \theta_4} - \frac{\partial m_{34}}{\partial \theta_2} + \frac{\partial m_{24}}{\partial \theta_3} \\ &= -m_4 a_2 l_4 sin\theta_{34} - 2m_4 a_3 l_4 sin\theta_4 \\ &\quad - m_4 a_2 l_4 sin\theta_{34} \end{aligned} \tag{3.41}$$

Substituting the coefficients in Equation 3.30;

$$\begin{aligned} \tau_2 &= m_{22}\ddot{\theta}_2 + m_{23}\ddot{\theta}_3 + m_{24}\ddot{\theta}_4 \\ &\quad + \left[B_{23}\dot{\theta}_3^2 + B_{24}\dot{\theta}_4^2 + \gamma_{223}\dot{\theta}_2\dot{\theta}_3 + \gamma_{224}\dot{\theta}_2\dot{\theta}_4\right. \\ &\quad \left. + \gamma_{234}\dot{\theta}_3\dot{\theta}_4\right] \end{aligned} \tag{3.42}$$

- For the third DoF,

$$B_{31} = B_{33} = 0 \tag{3.43}$$

$$\begin{aligned} B_{32} = \frac{\partial m_{23}}{\partial \theta_2} - \frac{1}{2}\frac{\partial m_{22}}{\partial \theta_3} \\ = m_3 a_2 l_3 sin\theta_3 \\ + m_4(a_2 a_3 sin\theta_3 + a_2 l_4 sin\theta_{34}) \end{aligned} \tag{3.44}$$

$$B_{34} = \frac{\partial m_{34}}{\partial \theta_4} - \frac{1}{2}\frac{\partial m_{44}}{\partial \theta_3} = -m_4 a_3 l_4 sin\theta_4 \tag{3.45}$$

$$\gamma_{312} = \gamma_{313} = \gamma_{314} = \gamma_{323} = 0 \tag{3.46}$$

$$\gamma_{324} = \frac{\partial m_{32}}{\partial \theta_4} - \frac{\partial m_{24}}{\partial \theta_3} + \frac{\partial m_{34}}{\partial \theta_2} = -2m_4 a_3 l_4 sin\theta_{34} \tag{3.47}$$

$$\gamma_{334} = \frac{\partial m_{33}}{\partial \theta_4} - \frac{\partial m_{34}}{\partial \theta_3} + \frac{\partial m_{34}}{\partial \theta_3} = -2m_4 a_3 l_4 sin\theta_4 \tag{3.48}$$

Substituting the coefficients in Equation 3.30;

$$\begin{aligned} \tau_3 = m_{23}\ddot{\theta}_2 + m_{33}\ddot{\theta}_3 + m_{34}\ddot{\theta}_4 + B_{32}\dot{\theta}_2^2 + B_{34}\dot{\theta}_4^2 + \gamma_{324}\dot{\theta}_2\dot{\theta}_4 + \\ \gamma_{334}\dot{\theta}_3\dot{\theta}_4 \end{aligned} \tag{3.49}$$

- For the fourth DoF;

$$B_{41} = B_{44} = 0 \tag{3.50}$$

$$B_{42} = \frac{\partial m_{24}}{\partial \theta_2} - \frac{1}{2}\frac{\partial m_{22}}{\partial \theta_4} = m_4(a_2 l_4 sin\theta_{34} + a_3 l_4 sin\theta_4) \tag{3.51}$$

$$B_{43} = \frac{\partial m_{34}}{\partial \theta_3} - \frac{1}{2}\frac{\partial m_{33}}{\partial \theta_4} = m_4 a_3 l_4 sin\theta_4 \tag{3.52}$$

$$\gamma_{412} = \gamma_{413} = \gamma_{414} = \gamma_{424} = \gamma_{434} = 0 \tag{3.53}$$

$$\gamma_{423} = \frac{\partial m_{42}}{\partial \theta_3} - \frac{\partial m_{23}}{\partial \theta_4} + \frac{\partial m_{34}}{\partial \theta_2} = 2m_4 a_3 l_4 sin\theta_4 \tag{3.54}$$

Finally, for the last joint equation of motion is written in Equation 3.55;

$$\tau_4 = m_{24}\ddot{\theta}_2 + m_{34}\ddot{\theta}_3 + m_{44}\ddot{\theta}_4 + B_{42}\dot{\theta}_2^2 + \gamma_{423}\dot{\theta}_2\dot{\theta}_3 \tag{3.55}$$

Analytical dynamic model of SHAD robot is verified using SimMechanics model. Methodology of the verification is configured as running SimMechanics model of the robot along with the analytical model in the same simulation using same initial conditions and for the same trajectory, which provides comparable outputs in terms of force (N) and torque (N.m) calculated for the joint actuator inputs to the system. It should be noted that

SimMechanics model is run in kinematics mode which means that the joint actuators are fed motion information. In this way, possible error contributions due to the controller performance in dynamic mode is eliminated. Initial conditions of joint space coordinates for simulations tests are selected so that robot's end-effector is positioned at 1300, 0 ,1000 mm in x-, y- and z-directions respectively in task space. The values of joint coordinates are 1000 mm, -60^o, 81,787^o and 38,123^o for S_1, θ_2, θ_3 and θ_4, respectively. Using this initial set, a desired trajectory for moving simultaneously 350 mm in (+) x-, y- and z-direction is designed, and corresponding joint motions are calculated by the inverse kinematics solutions for the redundant robot operation presented in this Chapter.

In the simulation, force and torque values for all joints are obtained using both models to be compared to each other. The procedure of this simulation tests is presented as a flowchart in Figure 3.5. Finally, results of this comparison are provided using force, and torque graphs, and force and torque errors plots in Figure 3.6 and Figure 3.7, respectively.

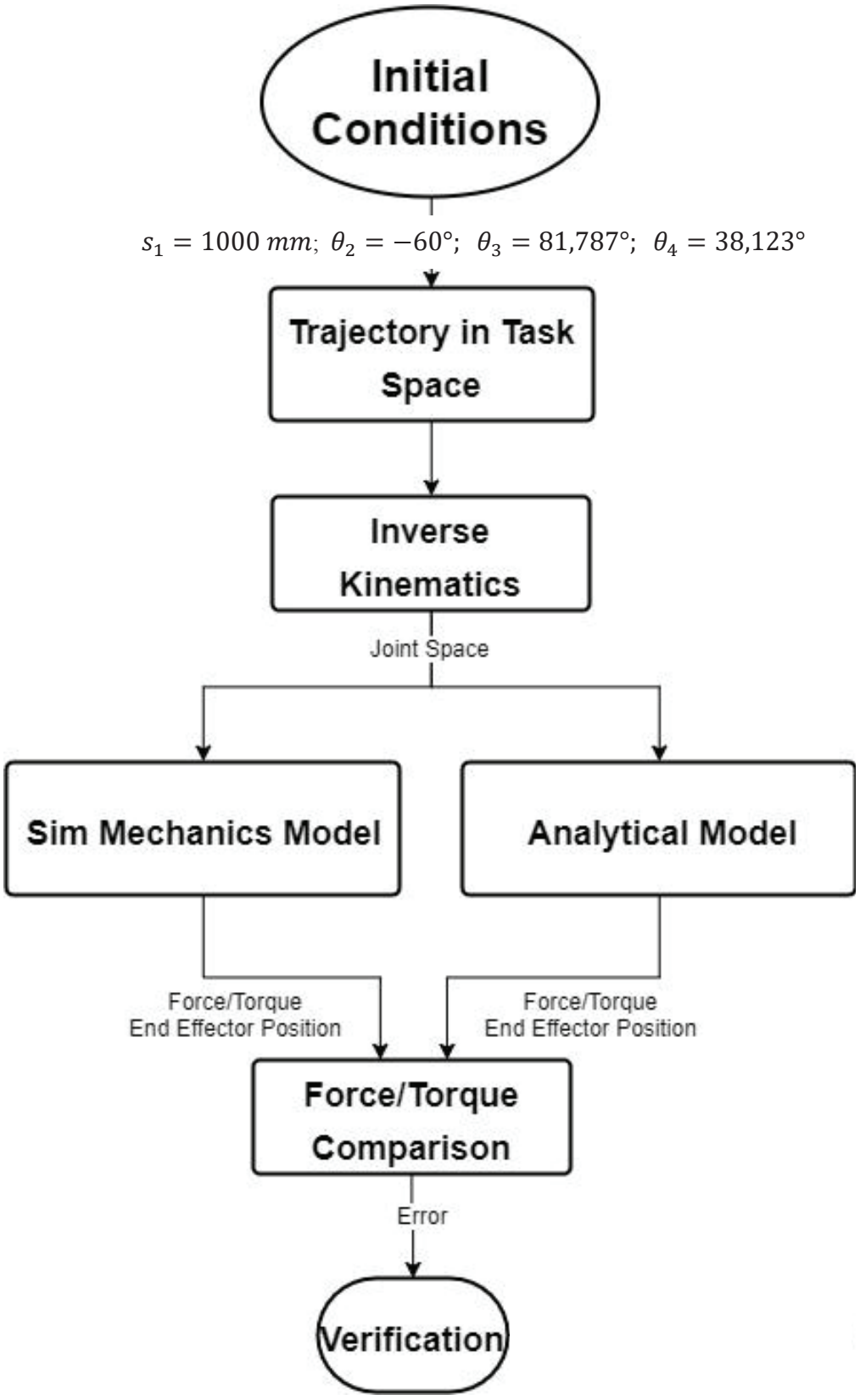

Figure 3.5. Verification of dynamic model

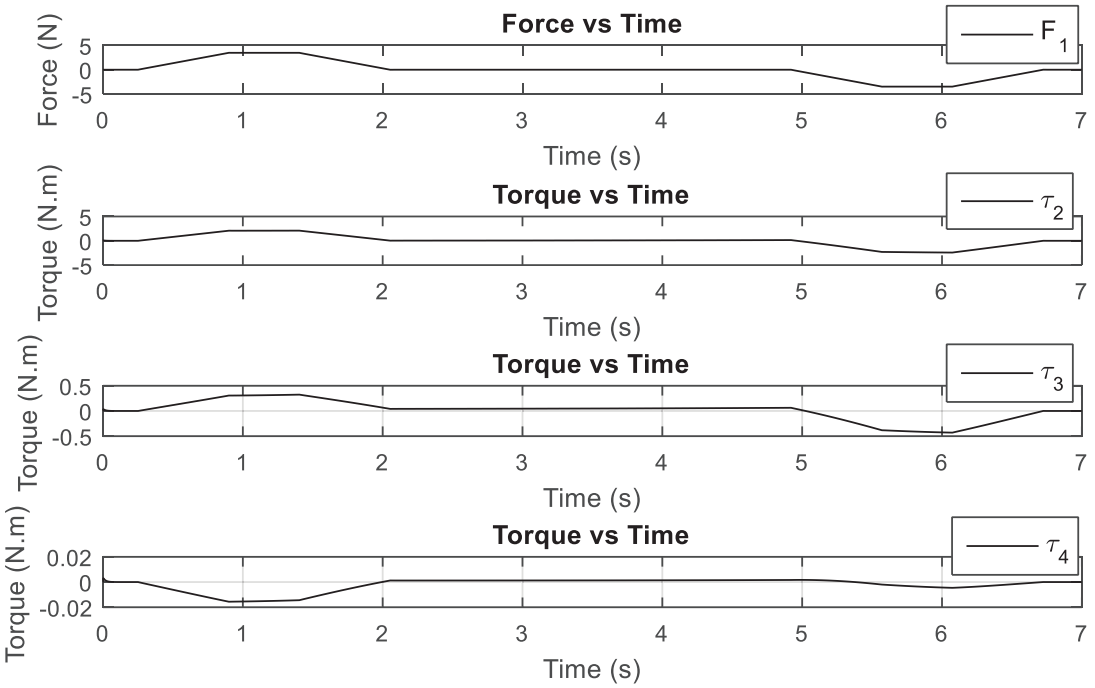

Figure 3.6. Force / torque values of joints

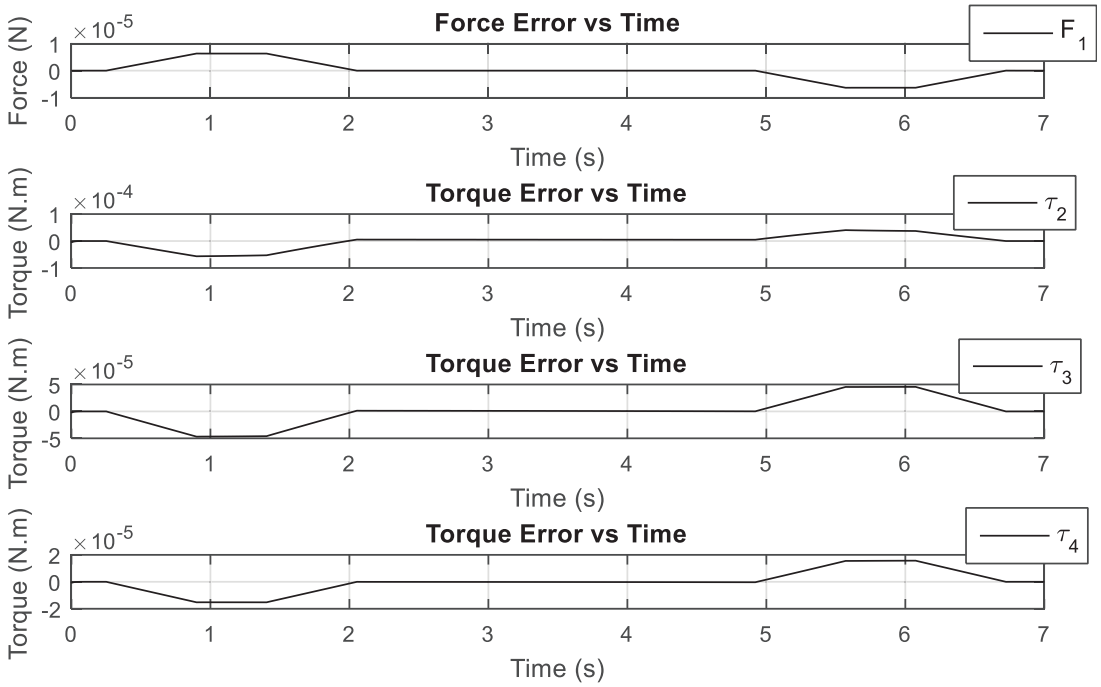

Figure 3.7. Force / torque errors of joints

When a trapezoidal acceleration trajectory for the end-effector motion is specified:

- For the 1st joint: SimMechanics model result in a trapezoidal force which has peaks of +3,4823 N in acceleration phase and -3,4823 N in deceleration phase of the motion. For the same motion analytical model gives neighbouring results with errors of $\pm 6{,}3522 \times 10^{-6}$ N in acceleration and deceleration compared to the SimMechanics results.
- For the 2nd joint, SimMechanics model result in a trapezoidal torque which has peaks of +2,0898 Nm in acceleration and -2,4187 Nm in deceleration phase of the motion. For the same motion analytical model gives neighbouring results with errors of $-4{,}043 \times 10^{-6}$ Nm in acceleration and $+5{,}6656 \times 10^{-5}$ Nm in deceleration compared to the SimMechanics results.
- For the 3rd joint, SimMechanics model result in a trapezoidal torque which has peaks of +0.3241 Nm in acceleration and -0.4294 Nm in deceleration phases of the motion. For the same motion analytical model gives neighboring results with errors of $-4{,}551 \times 10^{-5}$ Nm in acceleration and $+4{,}683 \times 10^{-5}$ Nm in deceleration compared to the SimMechanics results.
- For the 4th joint, SimMechanics model result in a trapezoidal torque which has peaks of -0.003 Nm in acceleration and -0.0045 Nm deceleration zones of the motion. For the same motion analytical model gives neighboring results with errors of -1.521×10^{-5} Nm in acceleration and $+ 1.557 \times 10^{-5}$ in deceleration compared to the SimMechanics results.

Table 3.3 shows the maximum force and torque values in acceleration and deceleration zones. Also, the maximum force and torque errors in these zones are given in Table 3.3.

Table 3.3. Maximum, minimum force / torque values and errors

Joint Number	Max. Force (N) / Torque (N.m) in acceleration zone	Max. Force (N) / Torque (N.m) in deceleration zone	Max. error in acceleration zone (N and Nm)	Max. error in deceleration zone (N and Nm)
1	3,4823 N	-3,4823 N	$6{,}3522 \times 10^{-6}$ N	$-6{,}3522 \times 10^{-6}$ N
2	2,0898 Nm	-2,4187 Nm	$-4{,}043 \times 10^{-6}$ Nm	$5{,}6656 \times 10^{-5}$ Nm
3	0,3242 Nm	-0,4294 Nm	$-4{,}551 \times 10^{-5}$ Nm	$4{,}6830 \times 10^{-5}$ Nm
4	-0,003 Nm	-0,0045 Nm	$-1{,}521 \times 10^{-5}$ Nm	$-1{,}557 \times 10^{-5}$ Nm

As a result of these simulation tests, analytical dynamic model of SHAD robot is verified via SimMechanics model. The differences in the results of this verification are acceptable within the tolerance bands of numerical errors. Therefore, the analytical model is proven to be viable for simulating control methods before experiments with the robot manipulator.

Initially, the derived dynamic model of SHAD is planned to be used in computed torque control method. In order to verify that it is possible to implement computed torque method for the control of actual SHAD system, torque control is tested on a single actuator via one driver. This work is given in detail in the next chapter.

CHAPTER 4

EXPERIMENTAL SETUP

In this chapter, primarily experimental setup and data flow between the components of the setup are presented. The drivers of the actuators have different modes of operation. One of the modes is torque control which can be used to implement computed torque method. Another mode of operation is the speed mode which can be used to directly feed in the speed demands to the actuators. In next section, experimental setup for torque mode and torque mode's test results are given and discussed. The following sections describe the speed mode of operation, and homing algorithm to bring the robot arms to their starting position.

4.1 Components of the Setup and Overview of Operation Modes

Experimental test setup is developed to run the controller tests on the SHAD robot. Control of the system is performed by using MATLAB/Simulink and Real-Time Windows Target. The components of the setup and information transfer scheme between the components are shown in Figure 4.1. As shown in Figure 4.1, Quanser Q8 DAQ is used for data transfer between with MATLAB and LS Mecapion drivers which are also called Servo Drives (SD). The controller outputs are generated in MATLAB Simulink, and the generated outputs are sent to SDs via DAQ. Measured position and force information are sent to the DAQ to be transmitted from DAQ to MATLAB. Control algorithms are run at a sampling rate of 1 kHz.

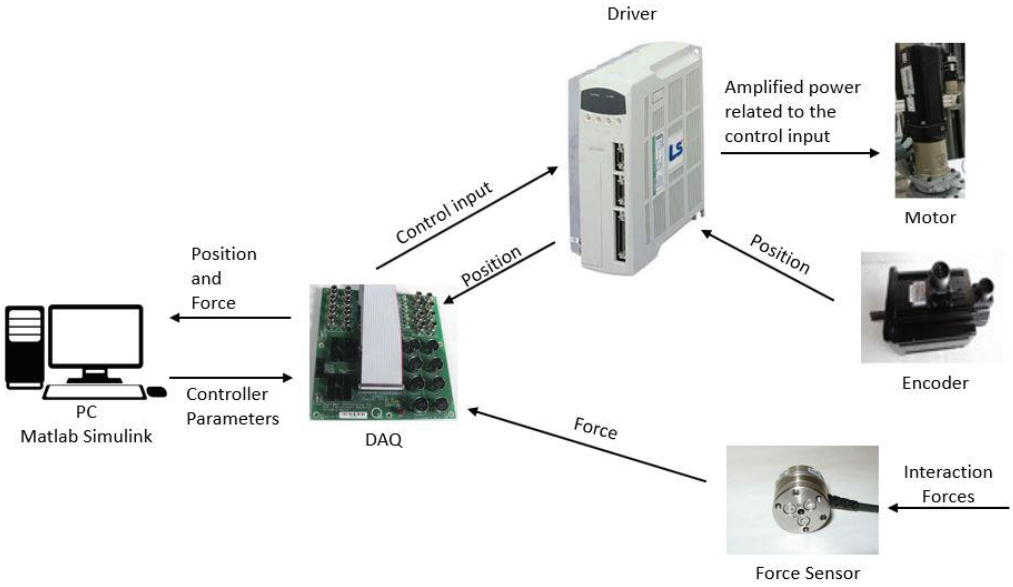

Figure 4.1. Information exchange scheme

The specification of DAQ are given in Table 4.1. DAQ is used for acquiring analog/digital signals that are sent from SDs and sent commands from host computer running MATLAB to SDs. 4 of the 8 quadrature encoder inputs are used for obtaining 4 encoders measurements. 4 of the 8 analog outputs are used for to send controller output data converted to the corresponding voltages to the 4 SDs. 3 of the 8 analog inputs are used to acquire data from the force sensor in 3 axes to measure forces in 3 axes as applied by the user. The connections of the electrical terminals which connects the SDs and DAQ are given in Appendix A.

Table 4.1. Specification of Quanser Q8

Item	Quantity	Property
Analog Inputs	8	14-bit
Analog Outputs	8	12-bit
Quadrature Encoder Inputs	8	
I/O Channels	32	Programmable
Dedicated Counter/ Timers	2	32-bit
Reconfigurable Encoder Counter/Timers	2	24-bit
PWM Inputs	2	

The component to be used for force measurement when running admittance control is ATI INDUSTRIAL AUTOMATION Nano 25 force sensor. The transducer is one of the smallest 6-axis transducers. The sensing ranges of Nano 25 are given in Table 4.2.

Table 4.2. Sensing ranges of Nano 25

Fx, Fy	Fz	Tx, Ty	Tz
125 N	500 N	3 Nm	3 Nm

The force sensor is located between the end-effector of the robot. To apply the force, the handle is fixed in front of the force sensor. The handle is mounted horizontally to the ground to reduce the pressure on user's wrist during the experiments. The length of the handle is 10 cm which is enough for a comfortable grip. Figure 4.2 shows the force sensor, handle and mounting of sensor and handle.

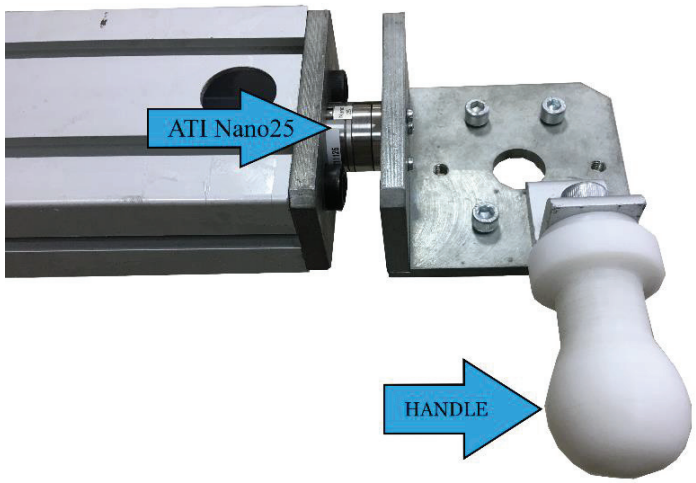

Figure 4.2. Force sensor and handle

According to the user manual of SDs, they are compatible for torque operation mode and speed operation mode which are aimed to be used in this study. The information about torque operation mode and speed operation mode are given in Figure 4.3 and Figure 4.4.

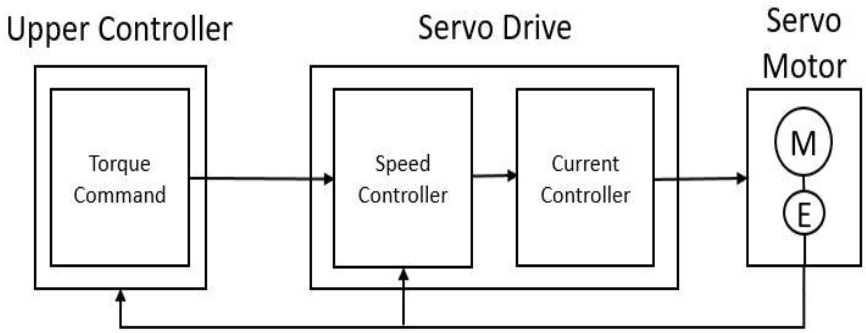

Figure 4.3. Torque operation mode

In Figure 4.3, the torque commands are calculated in MATLAB and they are sent to the SDs via DAQ. The signals in terms of torque commands are received by the SD's speed controller and converted to the corresponding signals for the current controller. The output of current controller is fed to the motor. As it is expressed in the user manual of SD, the strength of this operation mode is its fast response time. However, this mode of operation could not be used in this thesis study and the reasons for this is explained in the next sections.

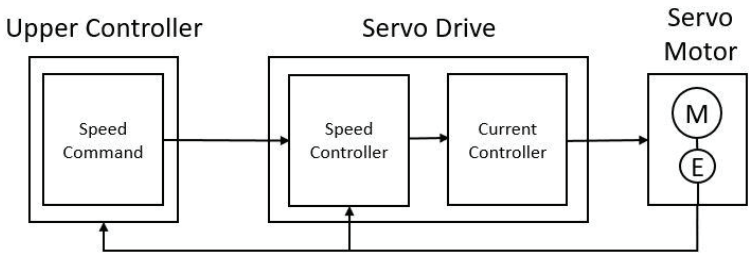

Figure 4.4. Speed operation mode

Speed operation mode is presented in Figure 4.4. In this mode, generated speed commands are sent to SDs. The generated signals are received by SD's speed controller and converted for current controller. The converted signal is fed to the motor. As it is expressed in the user manual of SD, the strengths of this operation mode are fast response time and easiness of precise control. This operation mode is used in this study since it has resulted in reliable operation as it is explained in the next sections.

4.2 Torque Control

In this section, tests are performed to determine whether the drivers are compatible with the torque mode. Experimental setup is shown in Figure 4.5. Experimental setup consists of torque sensor denoted with (1), motor denoted with (2) and SD denoted with (3). These components are listed with their brands and models in Table 4.3. During the experiments, SD is set to the torque mode and motor is driven in torque mode via analog signals sent from DAQ-MATLAB combination during the experiments. Meantime, the output shaft of the motor is coupled to the torque sensor, which is fixed to the inertial frame. In this way, corresponding torque values are measured for supplied reference inputs from MATLAB. Four experiments are carried out with different reference inputs.

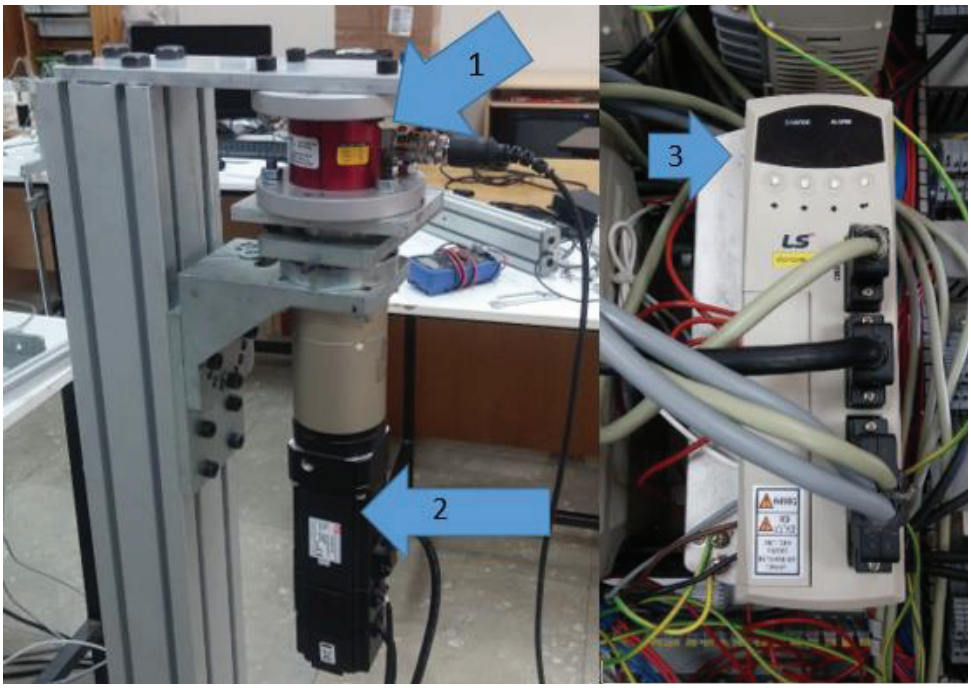

Figure 4.5. Torque mode test setup

Table 4.3. Torque Mode Test Setup Parts

Number	Device	Brand / Model
1	Torque Sensor	FUTEK TFF600
2	Servo Motor	LS AC (APM-SB04AEK2)
3	Servo Driver	LS VS04G4N-P1

Torque sensor is calibrated before experiments. Certain problems in the operation of the servo system are detected during measurements. First issue is the repeatability. In each experiment, the torque values are measured to have a relatively larger difference for the same reference input value. The next issue is that there is no linear relation or change between the reference input values and the measured torque. Another issue is that there is a considerable amount of change when the reference inputs are given in the opposite direction. The results are given as measured torque values from the torque sensor versus the analog reference inputs in Table 4.4 and Figure 4.6.

Table 4.4. Torque mode test results

Experiment 1		**Experiment 2**	
Torque Input (V)	Measured Torque (Nm)	Torque Input (V)	Measured Torque (Nm)
2	6,2	2	7,2
3	14,1	3	15,2
4	27	4	36,7
5	39,5	5	40,9
6	46	6	48
7	50,5	7	53
Experiment 3		**Experiment 4**	
Torque Input (V)	Measured Torque (Nm)	Torque Input (V)	Measured Torque (Nm)
2	8,1	-2	-19,5
3	11,5	-3	-23,5
4	17,4	-4	-28
5	26,4	-5	-33
6	29,2	-6	-44
7	42,2	-7	-61

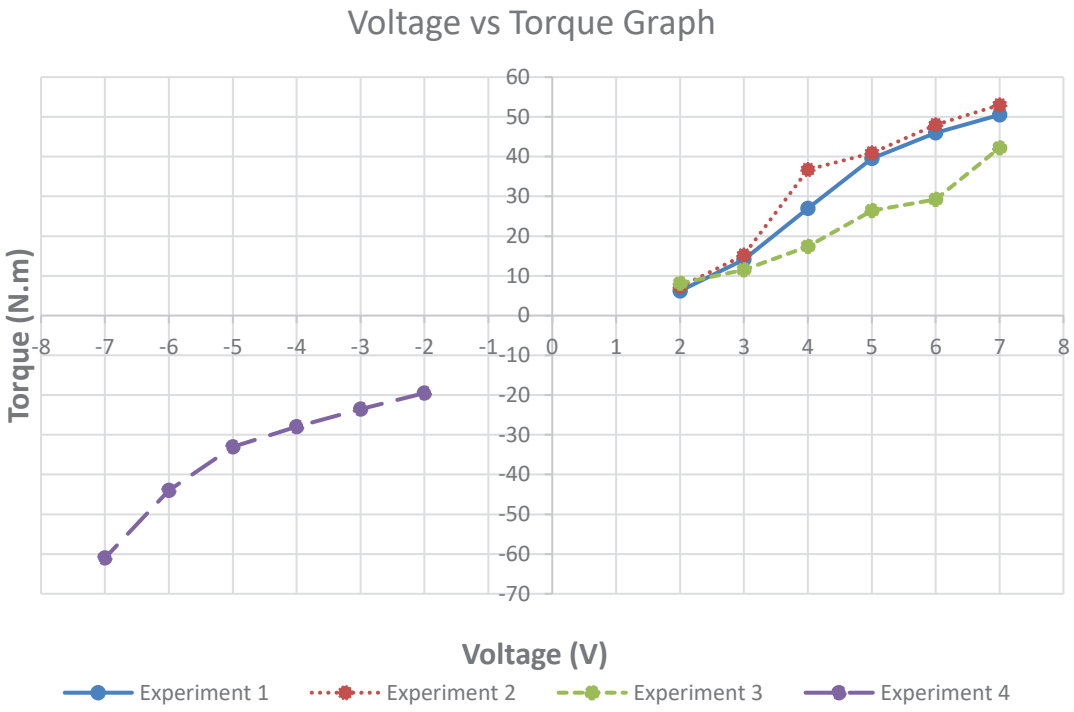

Figure 4.6. Torque mode test chart

The results show that SDs are not able to work in torque operating mode. Thus, drivers are set to speed operating mode for the rest of the experiments.

4.3 Speed Control

In this section, tests are executed to determine whether SDs are compatible with the speed operation mode. SD is set in speed mode and it is driven by analog signals sent from DAQ-MATLAB combination during the experiments. Four experiments are carried out at different reference values. Table 4.5 and Table 4.6 show the speed input values and measured speeds for four experiments. In these tests, the output shaft of the motor is not coupled to any other component and it is free to rotate.

Table 4.5. Speed mode test results for experiment 1 and 2

Experiment 1		Experiment 2	
Speed Input (v)	Measured Speed (deg/s)	Speed Input (v)	Measured Speed (deg/s)
0,1	1,7	0,1	1,7
0,2	3,4	0,2	3,41
0,3	5,05	0,3	5,02
0,4	6,75	0,4	6,75
0,5	8,43	0,5	8,42
0,6	10,16	0,6	10,18
0,7	11,9	0,7	11,9
0,8	13,63	0,8	13,67
0,9	15,34	0,9	15,35
1	17,3	1	17,3

Table 4.6. Speed mode test results for experiment 3 and 4

Experiment 3		Experiment 4	
Speed Input (v)	Measured Speed (deg/s)	Speed Input (v)	Measured Speed (deg/s)
-0,1	-1,67	-0,1	-1,68
-0,2	-3,4	-0,2	-3,4
-0,3	-5,14	-0,3	-5,15
-0,4	-6,92	-0,4	-6,96
-0,5	-8,62	-0,5	-8,62
-0,6	-10,38	-0,6	-10,4
-0,7	-12,08	-0,7	-12,08
-0,8	-13,85	-0,8	-13,86
-0,9	-15,5	-0,9	-15,53
-1	-17,25	-1	-17,26

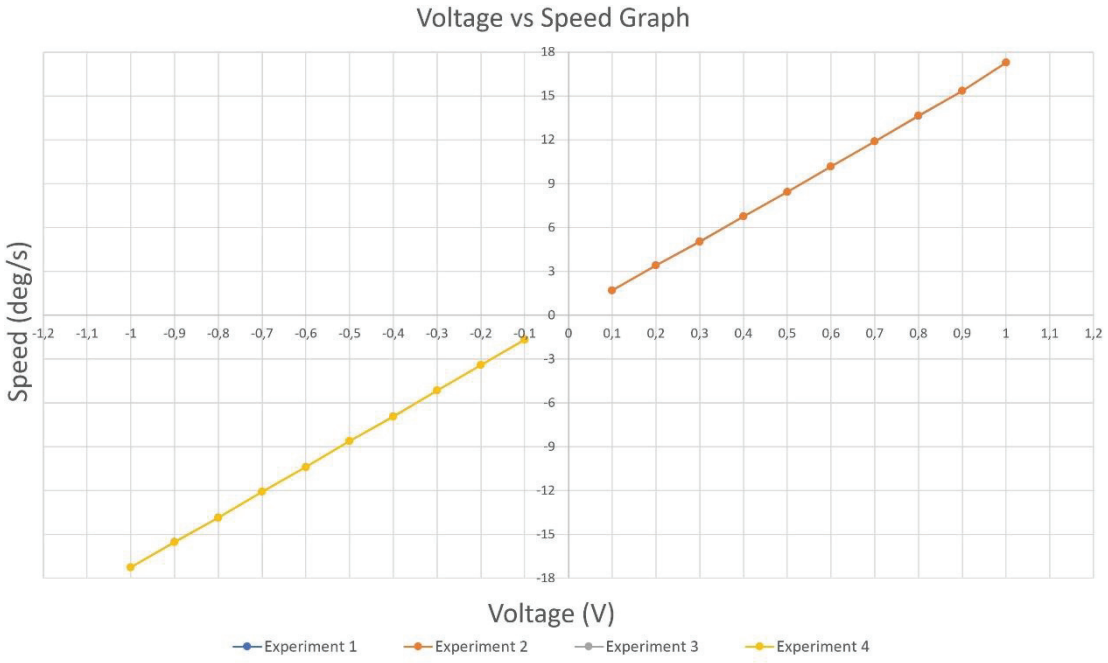

Figure 4.7. Speed mode test chart

Figure 4.7 shows the graph of the corresponding speed values for the reference inputs. As observed from the graph, the results of experiment 1 and experiment 2 overlap since they resulted in a very similar way, which indicates the repeatability is relatively good. Similarly, the results of experiment 3 and experiment 4 overlap.

The study in this section shows that problems observed in torque mode did not occur in speed mode. SDs are compatible for operation in speed mode.

Another vital pre-work for further experiments and applications of SHAD is finding home position also known as homing, which should be carried out before each controller test. This will ensure that robot always starts at a certain position, which is the initial position of the end-effector. Homing process is given in the next sub-section.

4.4 Homing Procedure

Since the SHAD robot has incremental encoders to measure the joint positions, there is a need of homing process. Homing means positioning the robot to its initial position after robot moved to an arbitrary position (Argyros et al., 2001).

In the study conducted by Dietrich et al. (2010), homing for parallel kinematic five-bar manipulators is described. The method for homing is joint based and need only homing switches. Thus, homing is taken place without human interaction. Also, they proposed mathematical relations to execute homing safely from any initial point. Safely in this case refers to avoiding from singularities and not violating workspace borders.

SHAD has 4 incremental rotary encoders. Since the incremental encoders are used in the device, it must be set to homing position before each operation. When the device is brought to the homing position, that means each axis is also brought to their respective homing positions. SHAD has 2 proximity sensors per link which totals up to 8 proximity sensors. SHAD's proximity sensors are inductive type sensors. To activate proximity sensors, metal plates are fixed between each link. Figure 4.8 shows proximity sensors and metal plate of a joint and 3D drawing of metal plate (Kanık et al., 2017).

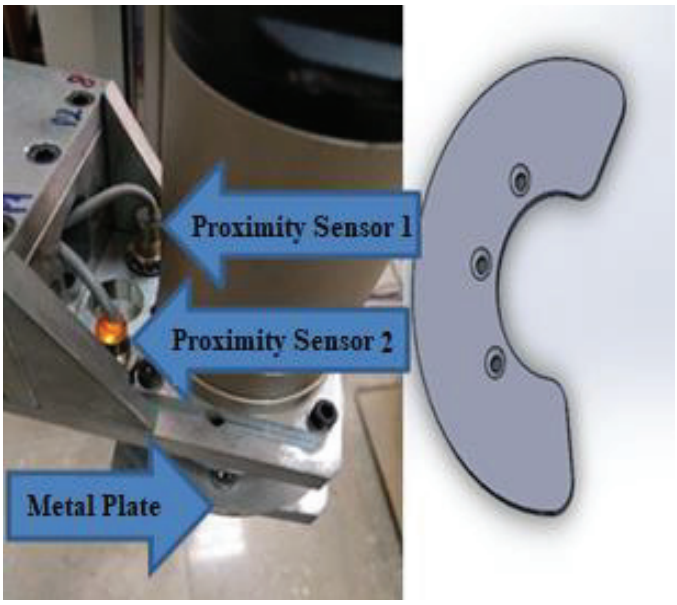

Figure 4.8. Proximity sensor, the metal plate and its 3D drawing

When the robot moves, each link has 4 combinations for sensors states except for the first link which is operated by the prismatic joint. First link has 3 combinations. The combinations are 1-1, 1-0, 0-1, 0-0 for the last three links and 0-0, 1-0, 0-1 for the first link. 1 and 0 represents the states of proximity sensors. 1 means that proximity sensor is on, 0 means off.

For homing process, homing is activated consecutively for each link starting from the first link and ending at the fourth link. The reason for this is that link lengths are relatively long and inertia is the highest on first link and the lowest on last link.

As the homing is initiated, system initially detects the states of the proximity sensors. For each state combination of the proximity sensors, algorithms are explained below and for each link it is repeated depending on initial condition of the states.

For the first joint, which is also prismatic joint, if the proximity sensors' states are 0-0, the respective actuator is driven to move upwards along the z-axis. When the prismatic axis reaches the top of the device, the states change to 1-0. At this state, position of the prismatic axis is set to 2m. If the sensors' states are 1-0, the prismatic axis position is set 2m and if the sensors' states are 0-1, the prismatic axis position is set to 0m. After the assignment of the prismatic axis position, the prismatic axis is moved to its selected initial position.

The homing algorithm is given in Figure 4.9 for four different states of the proximity sensors for the revolute joints of the robot. The developed algorithm is explained as follows;

- State 1-1: When proximity sensors' states are 1-1, link is rotated in positive direction until state becomes 1-0. When proximity sensors' state become 1-0, encoder data at that state is recorded (β_1). Following this, links is rotated in negative direction until states become 0-1. When proximity sensors' state become 0-1, encoder data is recorded (β_2). Since the angular position difference between these two states are known, raw encoder data is processed to set the middle position of these states to the 0° position of the link. Finally, link can be driven to the selected initial position for homing process.
- State 1-0: When proximity sensors' states are 1-0, link is rotated in negative direction until state becomes 1-1. When the proximity sensors' states become 1-1, encoder data at that state is recorded (β_1). Following this, link goes on rotating till the proximity sensor states become 0-1 and encoder data at that state is recorded (β_2). Since the angular position difference between these two states are known, raw encoder data is processed to set the middle position of these states to the 0° position of the link. Finally, link can be driven to the selected initial position for homing process.
- State 0-1: When proximity sensors' states are 0-1, link is rotated in positive direction until state becomes 1-1. When the proximity sensors' states become 1-1, encoder data at that state is recorded (β_1). Following this, link goes on rotating till the

proximity sensor states become 1-0 and encoder data at that state is recorded (β_2). Since the angular position difference between these two states are known, raw encoder data is processed to set the middle position of these states to the 0° position of the link. Finally, link can be driven to the selected initial position for homing process.

- State 0-0: When proximity sensors' states are 0-0, link is rotated in positive direction until state becomes 1-0. When proximity sensors' state become 1-0, encoder data at that state is recorded (β_1). Following this, link is rotated in negative direction until state becomes 1-0. When proximity sensors' state become 1-0, encoder data is recorded (β_2). Since the angular position difference between these two states are known, raw encoder data is processed to set the middle position of these states to the 0° position of the link. Finally, link can be driven to the selected initial position for homing process.

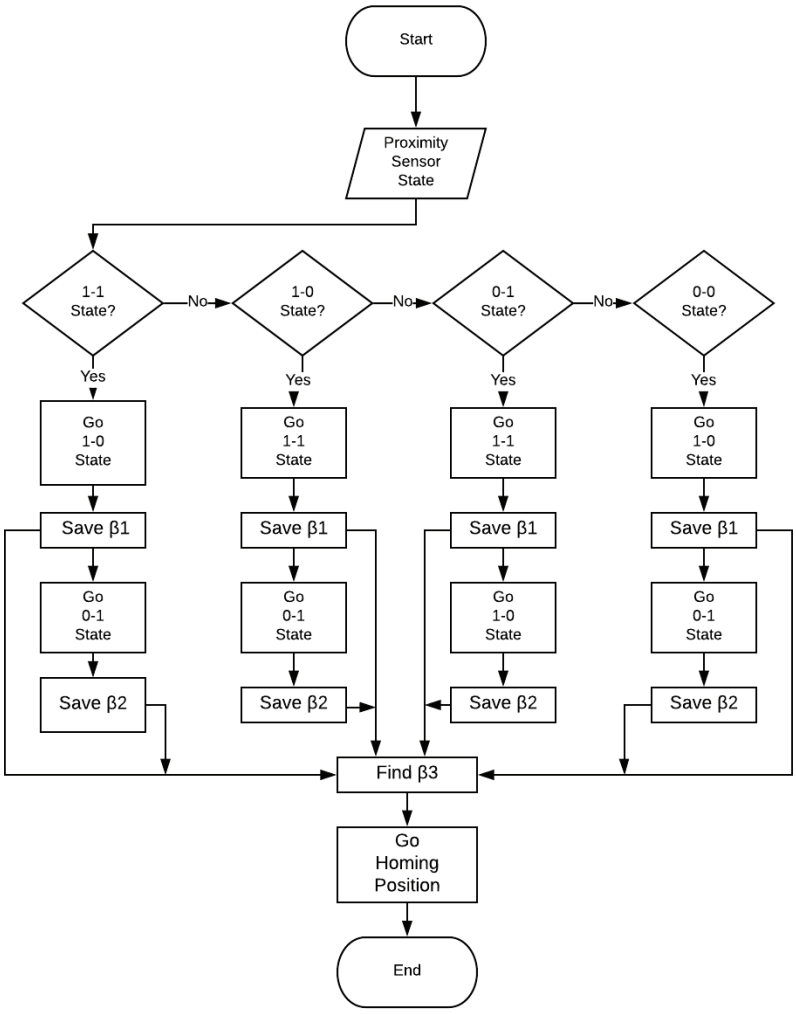

Figure 4.9. Homing flowchart

During the homing process, links are driven in speed mode operation. The necessary analog voltage signal that corresponds to the speed command is sent to SDs through the help of the algorithm and DAQ. The position information from the encoder is sent to DAQ via SD to be used in homing algorithm. The speed controller which is embedded in SD is shown in Figure 4.10. The controller is a proportional-integral (PI) controller with encoder feedback.

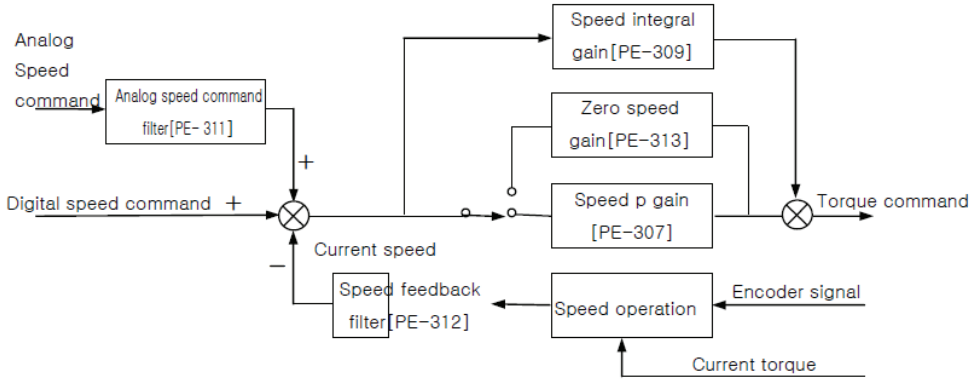

Figure 4.10. Embedded PI controller in servo driver

Using the desktop computer running MATLAB and DAQ, the speed commands are generated in the upper level with the help of a position control loop. Due to the noise existing in the system during the homing process of the robot arm, the robot arms rotate in negative direction. If this is not prevented, robot arm can cause damage to itself or surroundings. In order to prevent this unwanted rotation and move the robot arm to the desired position, a proportional control (P Control) is implemented in the upper controller as shown in Figure 4.11. The generated output signal is sent to embedded proportional-integral (PI) controller in SD.

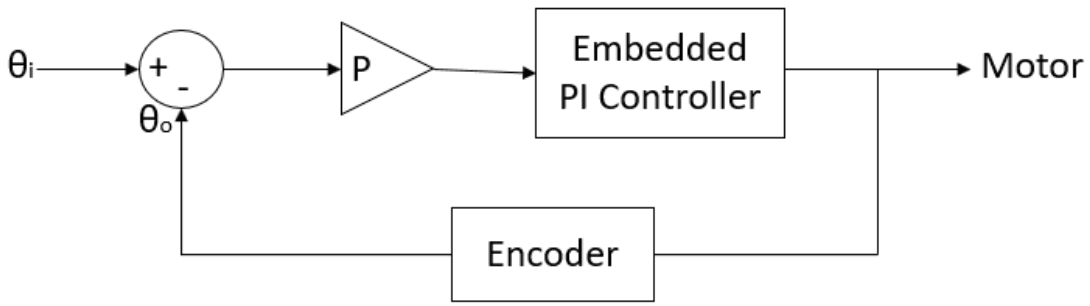

Figure 4.11. Upper P-control scheme

As a result of the homing process, robot's end-effector is moved to the selected initial position and it is now ready to receive any user command. It should be noted that the initial position of the robot is a selected one at (1.3, 0, 0.75 in m) and can be changed depending on the application needs.

CHAPTER 5

CONTROL ALGORITHMS AND THEIR TESTS

This chapter consists of description of the implemented control algorithms, simulation test results, and experimental test results. Before the experiments, control algorithms are implemented in MATLAB simulations. Later, the simulation algorithms are modified and applied in experiments to run experimental tests.

5.1 Control Algorithm for Obstacle Avoidance

Control algorithms illustrated in this section are designed for SHAD robot and implemented in SimMechanics model of SHAD and also the actual SHAD robot to test scenarios of position tracking with and without subtask. The SimMechanics model of SHAD has the identical kinematic and dynamic properties actual SHAD device. The physical properties of SHAD robot are acquired from 3D drawing of SHAD in Solidworks and translated to the Simulink model. The visual representation of SimMechanics model of SHAD is given in Figure 5.1 which also shows the obstacle identified as a black cylinder. SHAD's base is identified with a green bar which is also the sliding axis of the first joint which is the prismatic joint. Here, the prismatic joint is indicated by the red part which also carries the last three revolute axes of the robot that works on a plane.

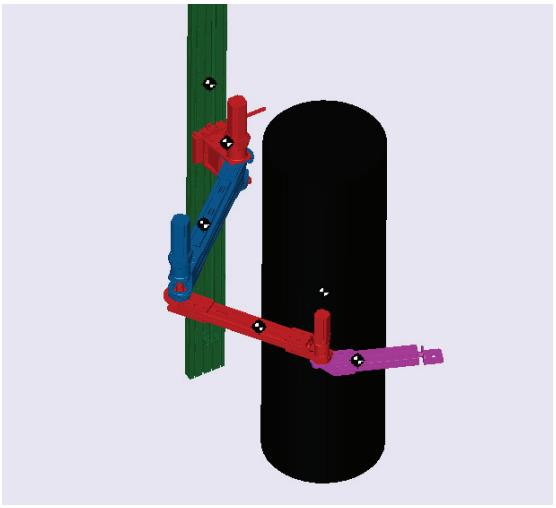

Figure 5.1. SimMechanics model of SHAD

SimMechanics model of SHAD is used to test the designed controller which is also used in the experiments with some modifications. The work scheme of this controller for position tracking is given in Figure 5.2.

Simulation and experiment tests are executed using same inputs for position tracking, therefore, this input must be compatible with the actual robot. To do that, inputs are smoothened using S-curve motion profile in velocity level via trapezoidal acceleration inputs. As given in the working scheme in Figure 5.2, acceleration input is supplied to the system and desired velocity is obtained via integration. The top-level controller is selected as a velocity feedforward proportional controller performed in the task space and the controller output, $\bar{\omega}_{CMD}$, is formulated in Equation 5.1. Initial condition of the end-effector position, $\bar{X}_i$, is modified via the integrated velocity demand signal, $\bar{X}_d = \int \bar{V}_d$. Respectively the error signal, $\bar{e}$, is generated as shown in Equation 5.2. The error signal is amplified by a diagonal $\hat{k}_p$ proportional gain matrix.

$$\bar{\omega}_{CMD} = \hat{J}^*\left(\bar{V}_d + \hat{k}_p \bar{e}\right) \tag{5.1}$$

$$\bar{e} = (\bar{X}_i + \bar{X}_d) - \bar{X} \tag{5.2}$$

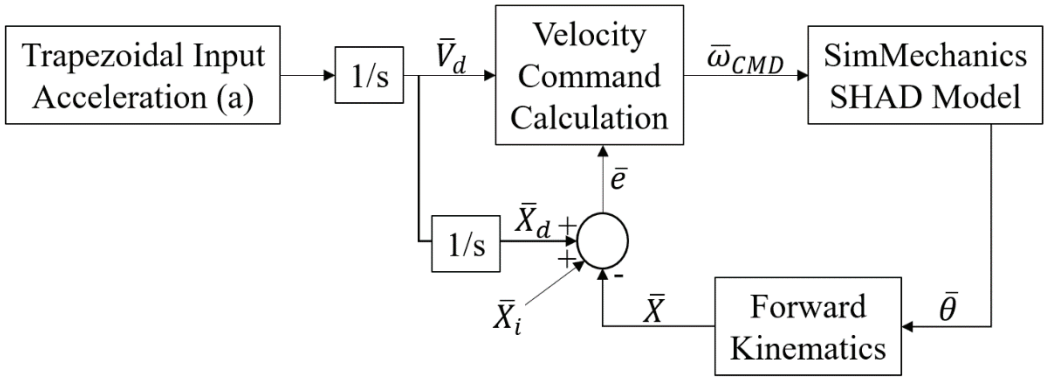

Figure 5.2. Motion trajectory tracking scheme in simulation

This controller is modified for calculating angular velocity command in the presence of a subtask as presented in Equation 5.3.

$$\bar{\omega}_{CMD} = \hat{J}^*\left(\bar{V}_d + \hat{k}_p \bar{e}\right) + \bar{f}_n \tag{5.3}$$

Difference between Equation 5.1 and Equation 5.3 is the auxiliary signal, $\bar{f}_n$, which is calculated using Equation 5.4.

$$\bar{f}_n = (\hat{I} - \hat{J}^* \hat{J}_r)\bar{g} \tag{5.4}$$

In this equation, $\bar{g}$ is a column matrix of subtask signals which are functions of scalar subtask function y_a. $\bar{g}$ and y_a formulations are given in Equations 5.5 and 5.6 respectively (Tatlıcıoğlu et al.,2005).

$$\bar{g} = -k_g(\bar{J}_S{}^T(\hat{I} - \hat{J}^* \hat{J}_r))^T y_a \tag{5.5}$$

$$y_a = e^{-\gamma*(\sum_{i=1}^{3} U_i * D_i)} \tag{5.6}$$

$\bar{J}_S$ in Equation 5.6 is a column matrix and its components are calculated as $J_{S(i-1)} = \frac{\partial y_a}{\partial \theta_i}$ for $i = 2,3,4$. U_i in Equation 5.7 represents the weight of the D_i function which is calculated as the smallest distance of the links to the obstacle. Therefore, U_i changes dominance of keeping i^{th}arm away from the obstacle with respect to the others. D_i in Equation 5.6 is calculated as given in Equation 5.7, where $i = 1,2,3$ denotes the first, the second and the third link on the plane. In this equation, R_{obs} and R_A represent radius of the obstacle and width of the robot's arm, respectively. Therefore, controller works to increase D_i so that y_a decreases.

$$D_i = \frac{\sqrt{((Y_{obs} - Y_i) - \frac{Y_{(i+1)} - Y_i}{X_{(i+1)} - X_i}(X_{obs} - X_i))^2}}{\sqrt{1 + (\frac{Y_{(i+1)} - Y_i}{X_{(i+1)} - X_i})^2}} - (R_{obs} - 0.5 * R_A) \tag{5.7}$$

For the actual system, control algorithm presented in simulation test part is modified so that the suitable velocity command in joint space can be feed to the SDs. Figure 5.3 shows the control scheme of SHAD. An additional proportional controller is used to eliminate drift in joint coordinates of SHAD due to the noise in the transmitted velocity demands. In addition, a safety logic with proximity sensors is established for avoiding any collision of the arms. As mentioned in homing procedure section (Figure 4.8), signals of proximity sensors are acquired to check their states and if their states

become 0-0 at any point of the manipulation, which means that the joint violates its limits. Safety logic makes velocity command drop to zero in order to avoid a possible collision of links.

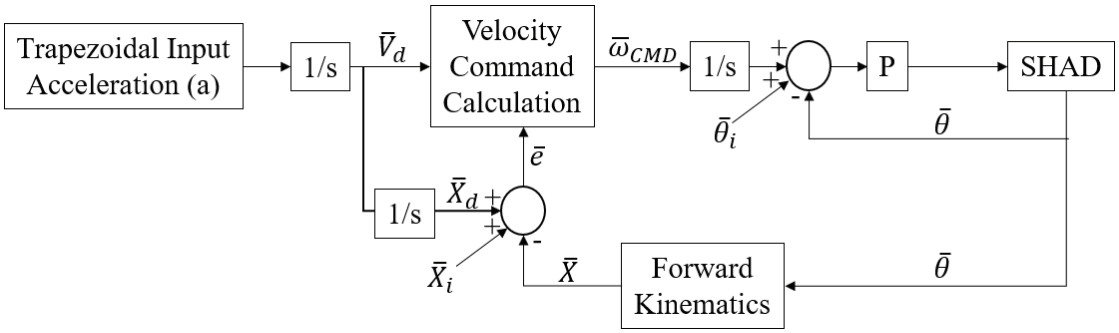

Figure 5.3. Motion trajectory tracking algorithm of SHAD in experiment

5.2 Control Algorithm for Admittance Control

This section describes the admittance controller devised for SHAD. Figure 5.4 shows admittance controller scheme implemented on SHAD. Since admittance controller is implemented only on the actual SHAD system and not on the simulation model, the control scheme is drawn to represent the working scheme of the admittance controller on the actual SHAD robot.

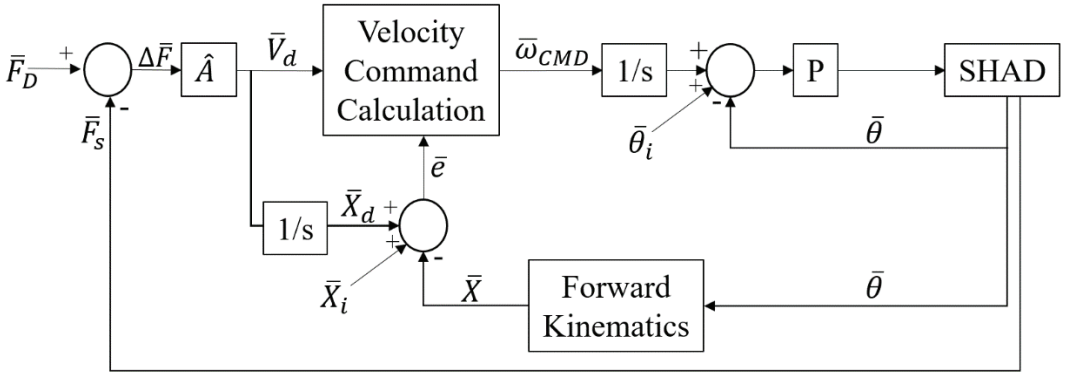

Figure 5.4. Admittance control of SHAD

An admittance control requires precise motion trajectory tracking. In contrast to the motion trajectory tracking algorithm described in the previous section, the motion trajectory tracking algorithm with obstacle avoidance subtask is used as the lower level

controller. In the upper level, the error calculated by comparing the desired force to be subjected to the user, $\bar{F}_D$, and measured force, $\bar{F}_s$, received from the force sensor is fed to the admittance term, $\bar{A}$, to generate the desired velocity of the end-effector. In this study, $\bar{F}_D$ value is selected as zero for full back-drivability and admittance term is modeled as;

$$\Delta\bar{F}(s) = \hat{m}s\bar{V}_{di}(s) + \hat{b}\bar{V}_{di}(s) \tag{5.8}$$

where;

$$\begin{aligned} \hat{m} &= diag(m_x, m_y, m_z) \\ \hat{b} &= diag(b_x, b_y, b_z) \end{aligned} \tag{5.9}$$

and corner frequency, ω_{c_i}, along any direction for first order admittance term is;

$$\omega_{c_i}, = \frac{b_i}{m_i} \text{ where } i = x, y, z \tag{5.10}$$

consequently, the admittance term, $A = diag(A_x, A_y, A_z)$, is calculated as;

$$\frac{V_{di}(s)}{\Delta F_i(S)} = \frac{1}{m_i s + b_i} = A_i \tag{5.11}$$

In Equation 5.8, ΔF_i represents force input to the admittance term for $i = x, y, z$, $\hat{m}$ represents mass matrix, V_{di} represents desired velocity as an output of the admittance term for $i = x, y, z$, $\hat{b}$ represents damper coefficients. In Equation 5.11 A_i represents admittance term designed for the i-direction motion where $i = x, y, z$. These mass and damper terms can be changed to set high or low admittance terms. If the admittance parameters are set to high values, higher force is required to move the robot. In this case, the robot becomes less reactive however, it is possible to execute relatively more precise movements. On the other hand, if the admittance parameters are set to low values, low force values will be enough to move the robot. However, this makes it difficult for precise control of the subsequent motion.

5.3 Simulation Test Results

This section provides the simulations test results which are executed in Simulink environment for evaluating the performance motion tracking without obstacle avoidance and motion tracking with obstacle avoidance subtask. Sequence of the tests are planned

so that, first, the controller is tested to verify if it can track desired task space trajectories without obstacle avoidance subtask. After that, the devised controller is tested while the robot tracks desired trajectory with obstacle avoidance subtask.

In these simulation tests, the obstacle is located in the task space at $[x, y] = [750,0]$ mm. The diameter of the obstacle is selected to be $R_A = 550$ mm and width of the links are all $R_{obs} = 90$ mm.

Results of SHAD's trajectory tracking with and without obstacle avoidance subtask in simulation tests are shown by end-effector's position error in workspace, the distance between links and obstacle, D_i, and subtask function, y_a.

Task space position trajectory calculated by using trapezoidal acceleration demand is presented in Figure 5.5. This trajectory is defined within the workspace limits and initial position of the robot end-effector is selected as $[x, y] = [1300,0]$ in mm. Since the redundant behavior of the robot is evaluated on the plane that is moved along the vertical axis by the prismatic joint, the location of the manipulator in z-axis is fixed.

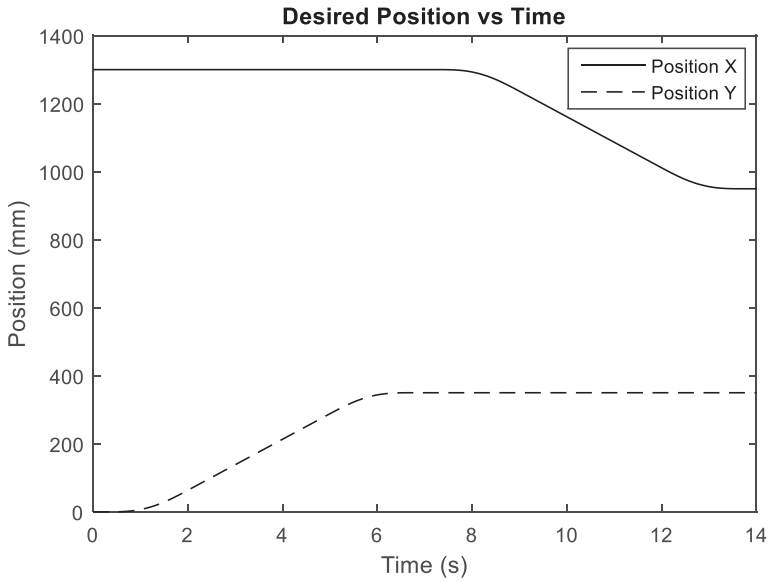

Figure 5.5. Position trajectory of the end-effector

First simulation test is the motion tracking of SHAD without obstacle avoidance subtask and Figure 5.6 shows motion tracking error of end-effector as a result of tracking desired trajectory given in Figure 5.5.

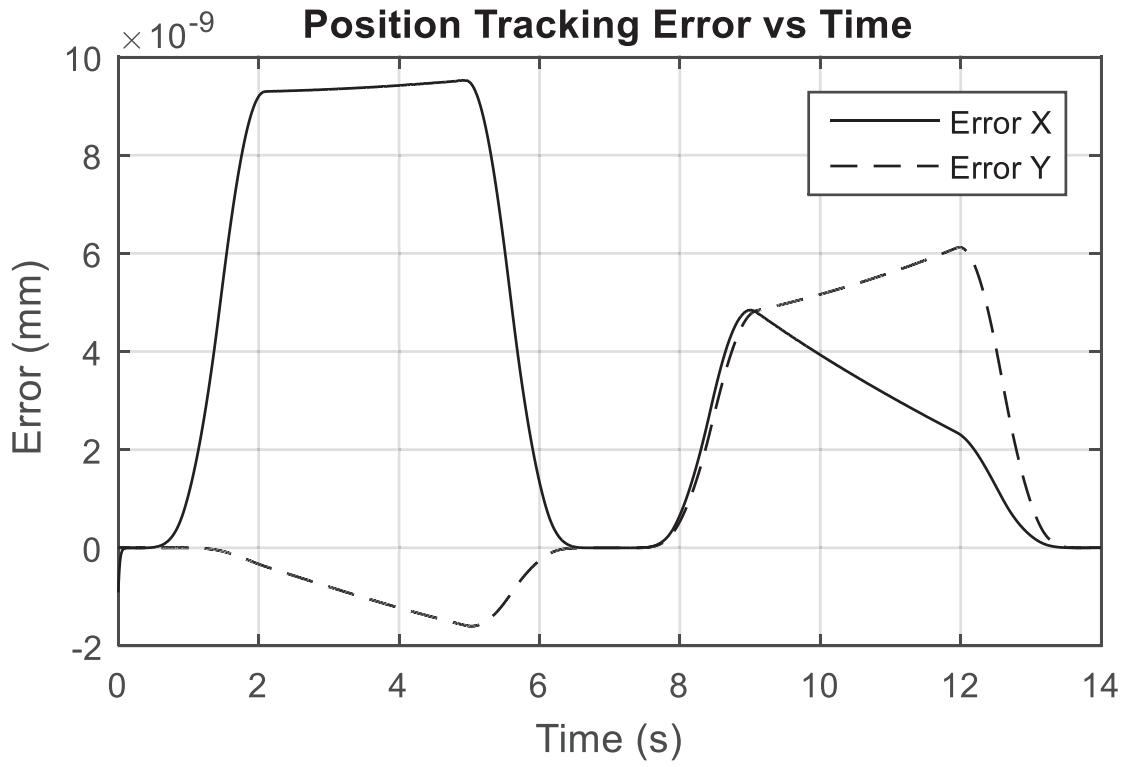

Figure 5.6. Position tracking error of end-effector without obstacle avoidance subtask

In Figure 5.6, maximum errors in x-axis and y-axis are observed as 1,952x10^{-8} mm 1,256x10^{-8} mm, respectively.

In Figure 5.7, the visualizations of SHAD robot during the simulation test are given for $t = 0,2,4,6,8,10,12,14$ s. In Figure 5.8, the distances, D_i, between links and obstacle, which is to be avoided in the next tests with obstacle avoidance subtask, are given.

Figure 5.7 indicates that SHAD collides with the obstacle while tracking its given trajectory. In this figure, second and third links of SHAD hit with the obstacle. The exact time of collision with the obstacle is obtained from Figure 5.8 by finding the time at the instant where related $D_i < 0$. According to this definition, second arm collides with obstacle at $t = 9.7$ s and enters in the obstacle by 56.65mm at the end of the desired trajectory. Third link collides at $t = 10.4$ s and enters in the obstacle by 106 mm at the end of the desired trajectory. It should be noted that the obstacle is a virtual body with no physical boundaries so that it cannot apply any force on the robot during this simulation.

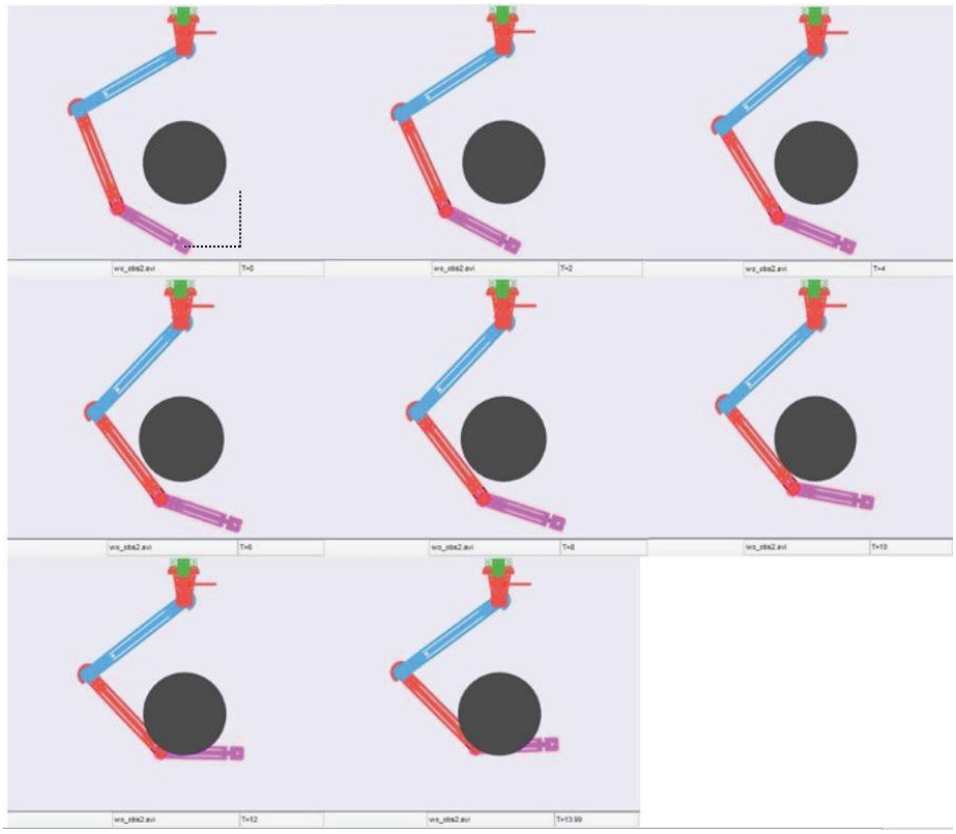

Figure 5.7. SHAD collides with the obstacle in simulation test without obstacle avoidance subtask

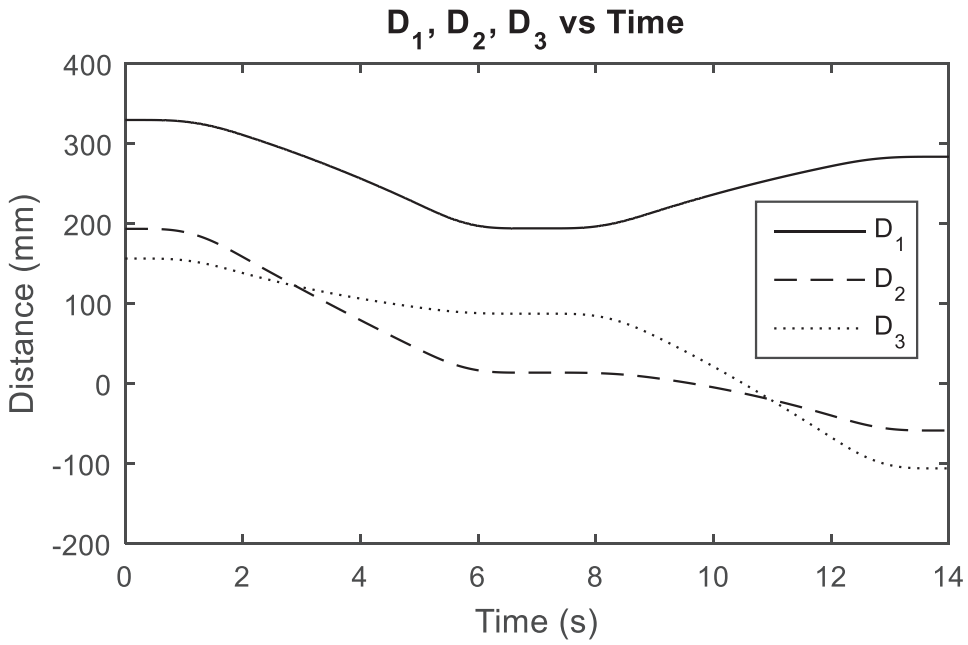

Figure 5.8. Distances of links from obstacle without obstacle avoidance subtask

The results of the second simulation test with obstacle avoidance subtask when the end-effector location is set to be fixed at $[x, y] = [1300,0]$ include positioning error in task space, values of distances of links of SHAD from the obstacle D_i, and subtask function y_a. Position error in task space, $\bar{e}$, change in the value of the subtask function, y_a, and the distances of the links from the obstacle, D_i, are presented in Figure 5.9, Figure 5.10 and Figure 5.11, respectively.

Figure 5.9 shows that SHAD's end-effector stays on the desired position, $[x, y] = [1300,0]$, with maximum errors of 4,9296x10^{-9} mm and 3,7395x10^{-9} mm in x and y axes, respectively. Since the subtask function, y_a, decreases exponentially to a lower value than its initial value as it is observed from Figure 5.10, it means that the subtask objective is met and links of SHAD has moved away from the obstacle.

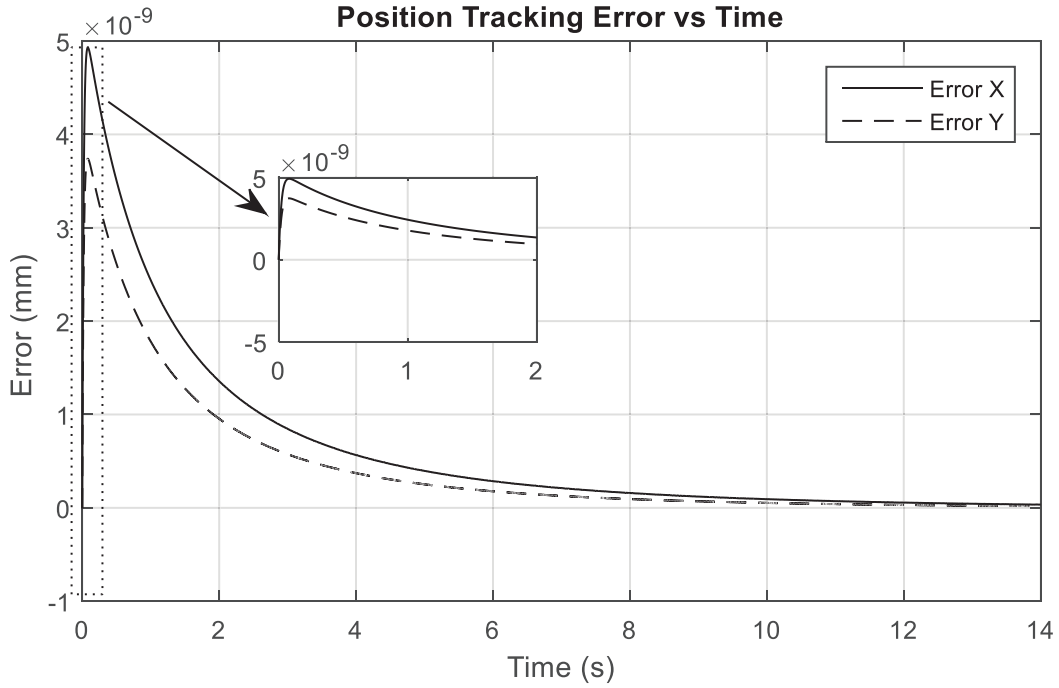

Figure 5.9. Position tracking error when end-effector fixed

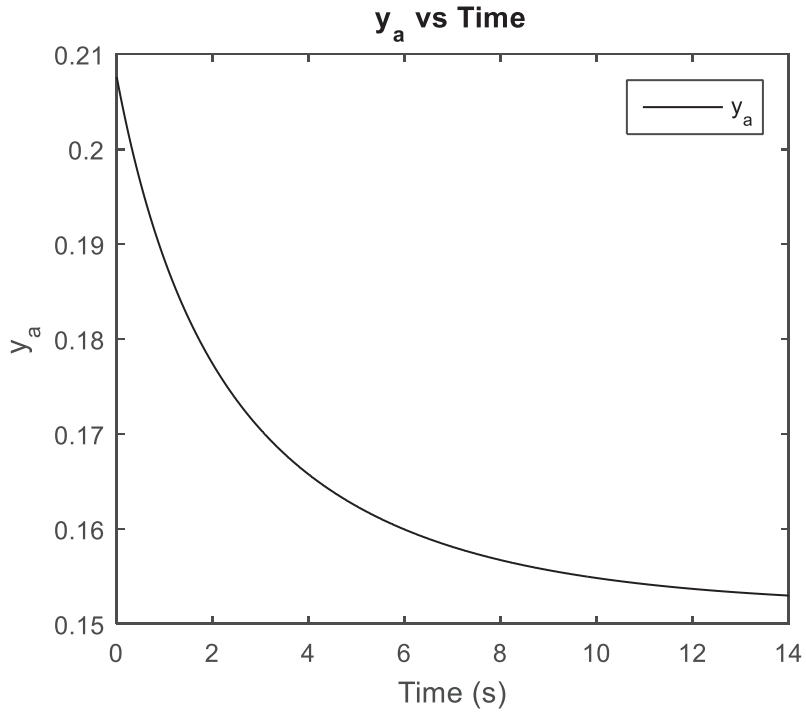

Figure 5.10. y_a vs time

Decreasing y_a indicates that summation of distances of arms from the obstacle multiplied with U_i weights, $\sum_{i=1}^{3} U_i * D_i$, has become larger. As a result, although some of the D_i values get smaller, summation of them increases with respect to the related weight gains and neither of them gets a negative value, which is observed in Figure 5.11.

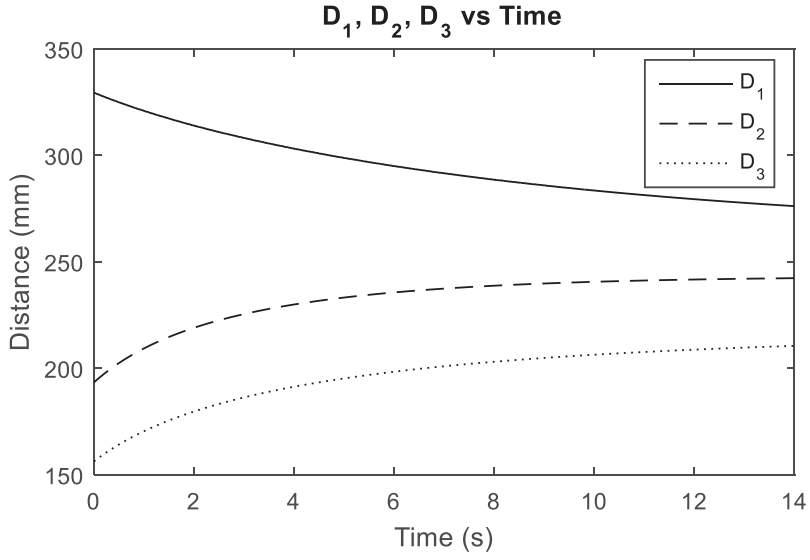

Figure 5.11. Distances of arms from the obstacle with obstacle avoidance algorithm when end-effector fixed

The same position trajectory given in Figure 5.5 is used for the next simulation test. This test is intended to show if subtask algorithm can move the arms of the SHAD away from the obstacle while executing the same position trajectory which resulted in the collision of the links with the obstacle. The results of this test are provided in Figure 5.12, Figure 5.13 and Figure 5.14. Figure 5.12 shows task space error during tracking the desired position trajectory. The range of errors are in the same scale of the results without the subtask at 10^{-9} mm ranges. It is observed from the screen shots presented in Figure 5.13 that SHAD does not collide with the obstacle.

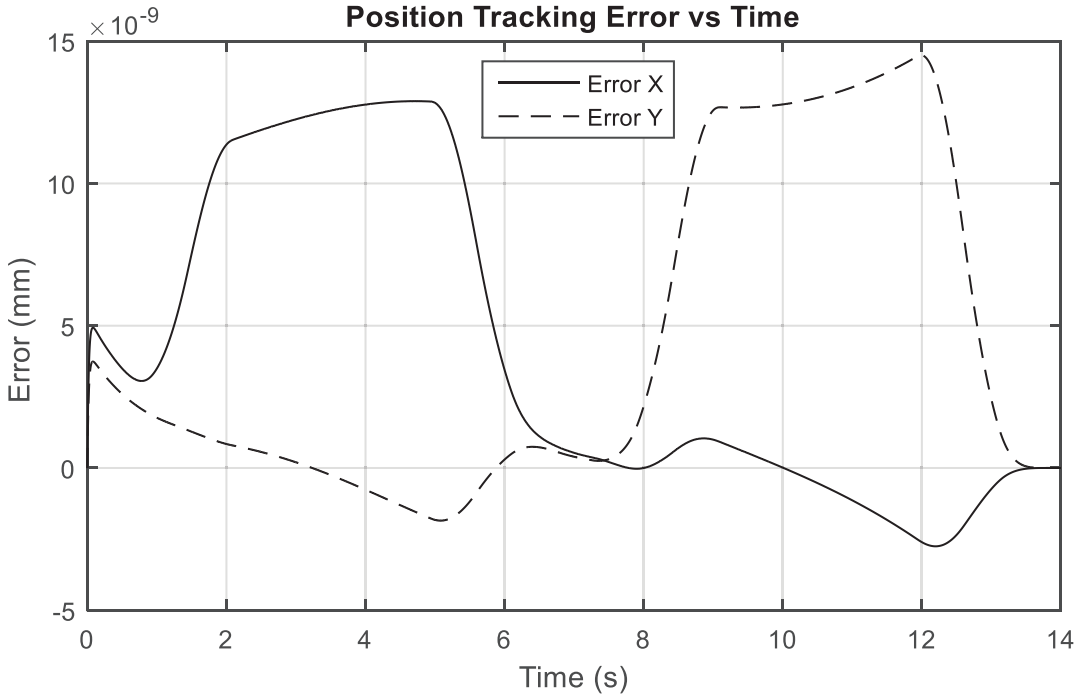

Figure 5.12. Position tracking error with obstacle avoidance subtask

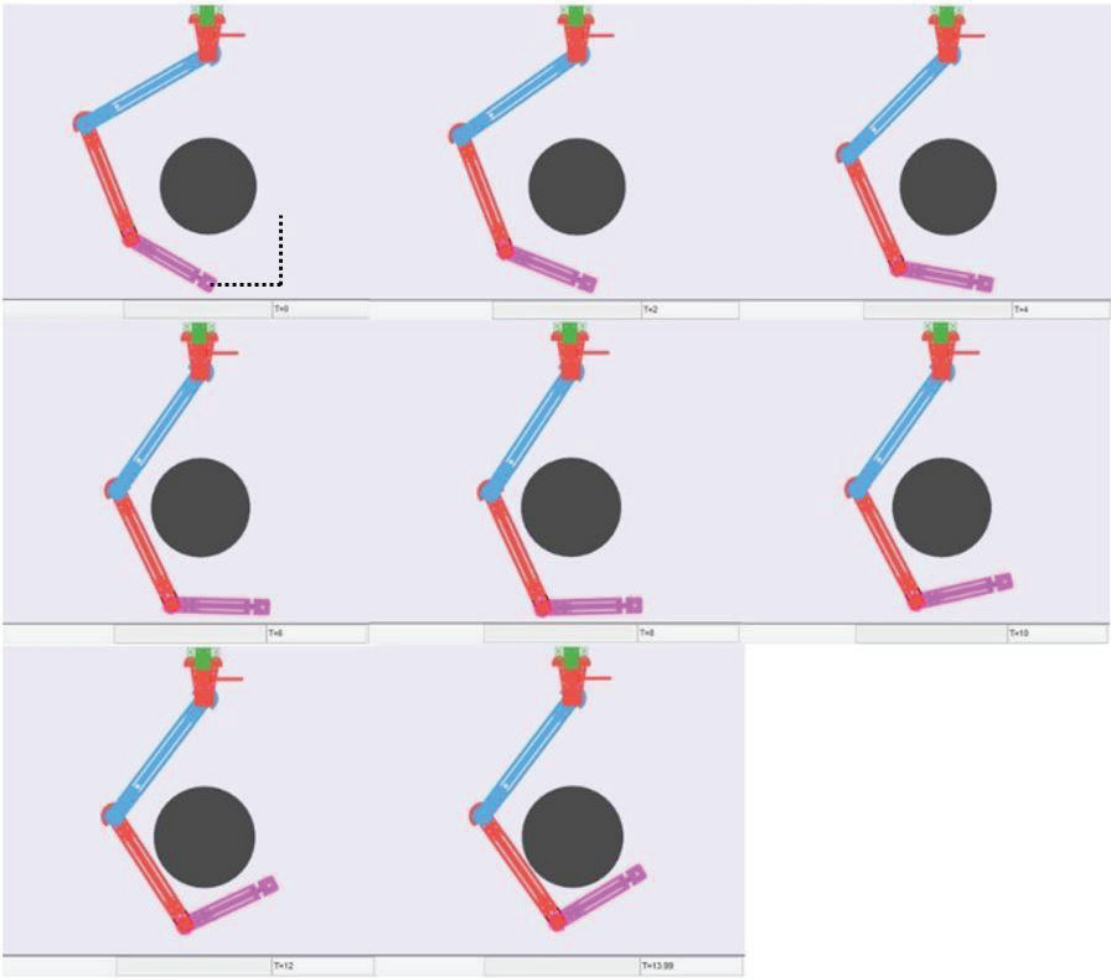

Figure 5.13. SHAD avoids from obstacle in simulation

According to robot configuration, D_i values vary between 329,5 mm and 156,3 mm in the beginning and vary between 134,5 mm and 9 mm at end of the simulation as provided in Figure 5.14. Although, D_i value receives smaller values through the end of the simulation test, they never receive negative values indicating that no collision has happened during the simulation. Figure 5.15 shows both subtask function, y_a, for the same trajectory given (in Figure 5.5) to the robot's end-effector when obstacle avoidance subtask is in use and obstacle avoidance subtask not in use. y_a is increasing 0.2 to 1.3 when obstacle avoidance subtask is not in use. On the other hand, y_a is increasing 0.2 to 0.7 when obstacle avoidance subtask is in use. According to algorithm, y_a tends to decrease, but due to given trajectory y_a is increasing. However, y_a is rising less when obstacle avoidance algorithm in use.

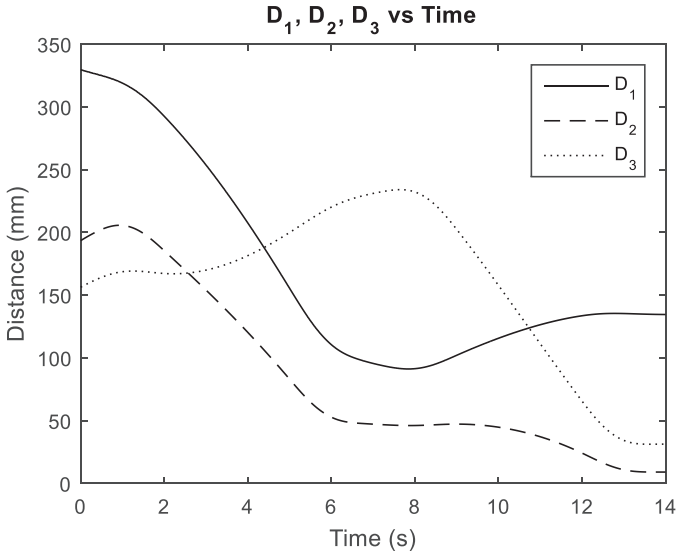

Figure 5.14. Distances of links from obstacle with obstacle avoidance algorithm

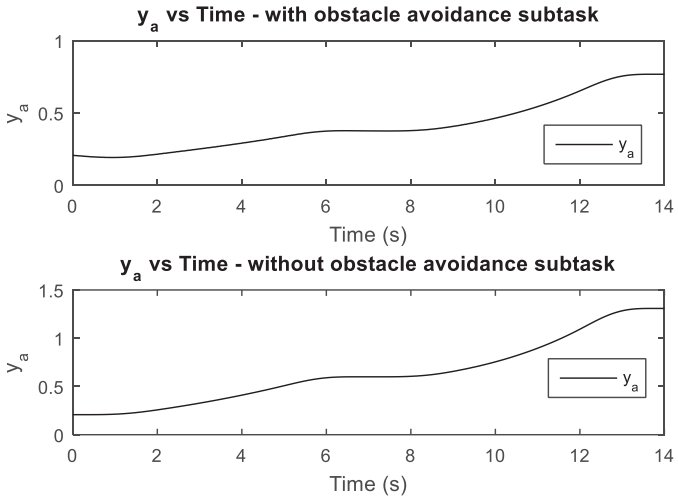

Figure 5.15. y_a vs time graphs when obstacle avoidance task in use and not in use

5.4 Experiments and Their Results

This section provides the experiments and the results of the tests executed with experimental test setup. The first experiment is carried out for evaluating the obstacle avoidance performance of the developed obstacle avoidance controller and the system while the robot end-effector tracks a given trajectory. The next set of tests are conducted to run the system by admittance controller. In these tests, a test procedure is defined and

followed to evaluate the effects of the parameters in admittance term when the robot is moved by a human operator via holding the handle attached to the robot's end-effector.

5.4.1 Obstacle avoidance experimental tests and results

Trajectory tracking with obstacle avoidance subtask test of SHAD is conducted for following the trajectory given in Figure 5.5. The results of the tests are obtained for position tracking error of SHAD in x and y directions and distances of arms from the obstacle's outer surface, D_i. This test is intended to show if subtask algorithm can move the arms of the SHAD away from the obstacle while tracking a given motion trajectory. The control algorithm scheme implemented on SHAD system in this experiment is presented in Figure 5.3. The obstacle used in these tests is the same obstacle defined in the simulation tests located at the same place in the task space.

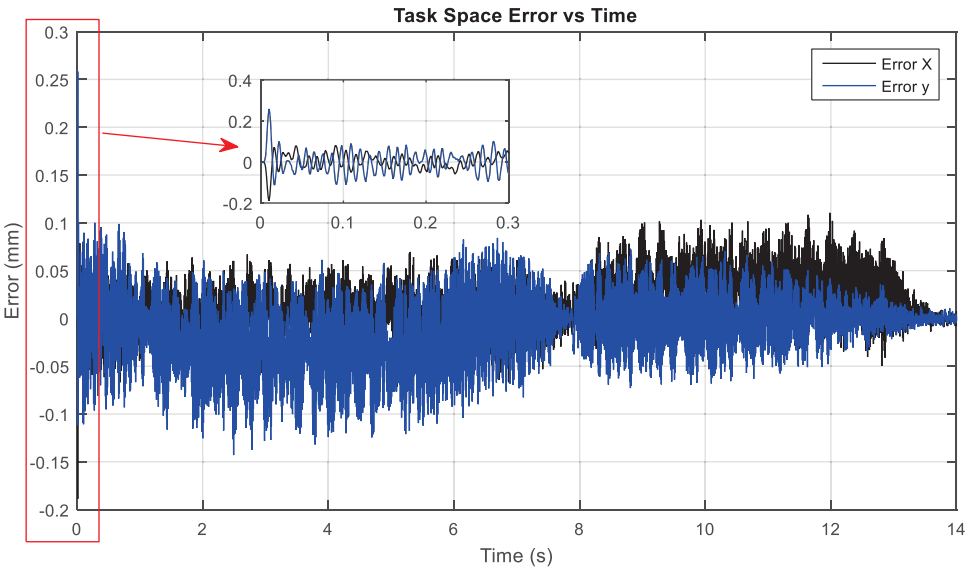

Figure 5.16. Task space position error of SHAD in experiment

Figure 5.166 shows motion trajectory tracking error of SHAD. It should be noted that the task space position of the end-effector is calculated in an indirect way by using the measured joint position in the forward kinematics formulas presented in Chapter 3. The maximum error calculated in x axis is 0.188 mm and in y axis is 0.258 mm. The distances of the links from the obstacle are shown in Figure 5.177.

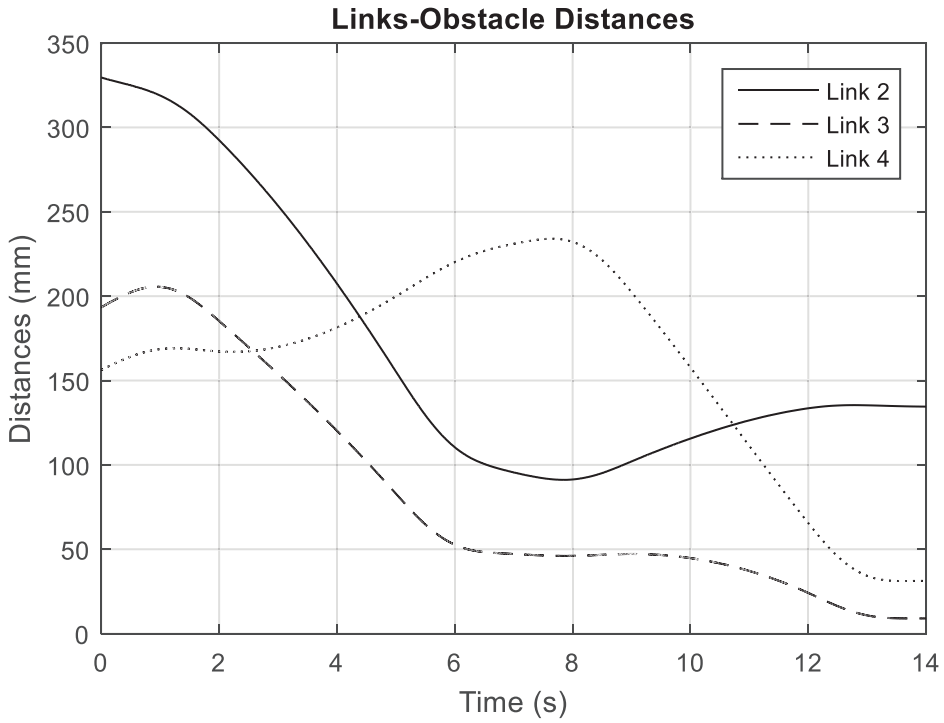

Figure 5.17. Distances of links from the obstacle during trajectory tracking

It is observed from Figure 5.177 that SHAD's links do not collide with the obstacle since the distance between the links and the obstacle has never dropped below zero. The closest distance is between any link and the obstacle during the whole test is 9 mm. The results obtained for the experimental tests and the simulation tests came out to be very similar to each other as expected.

5.4.2. Admittance control test and results

In this section, experiments are carried out to show the effects of parameter variation in admittance term. A test procedure is developed to observe the effort spent on a particular motion using different admittance terms and to see how accurate the human operator can perform the tasks with these admittance parameters. The working principle of the experimental setup is as follows;

- First of all, each subject is informed about the experiment.
- The human subject is located inside the workspace facing in the +x direction.
- Subject holds and moves the handle which is connected to the end-effector of the robot.

- The graphical user interface (GUI) indicates the location of the robot's end-effector during the experiment with a sphere.
- As subject applies force on the end-effector, these forces are measured by a force sensor and converted to motion demands in tasks space with respect to the selected admittance term.
- According to the generated motion demands, the robot is moved while avoiding the possible collisions between the links and the human subject, and the sphere in the GUI also moves accordingly.
- Motion of the sphere in the GUI provides visual feedback to the user about the task he/she performs.

The GUI observed by the subjects during the experiment is shown in Figure 5.188.

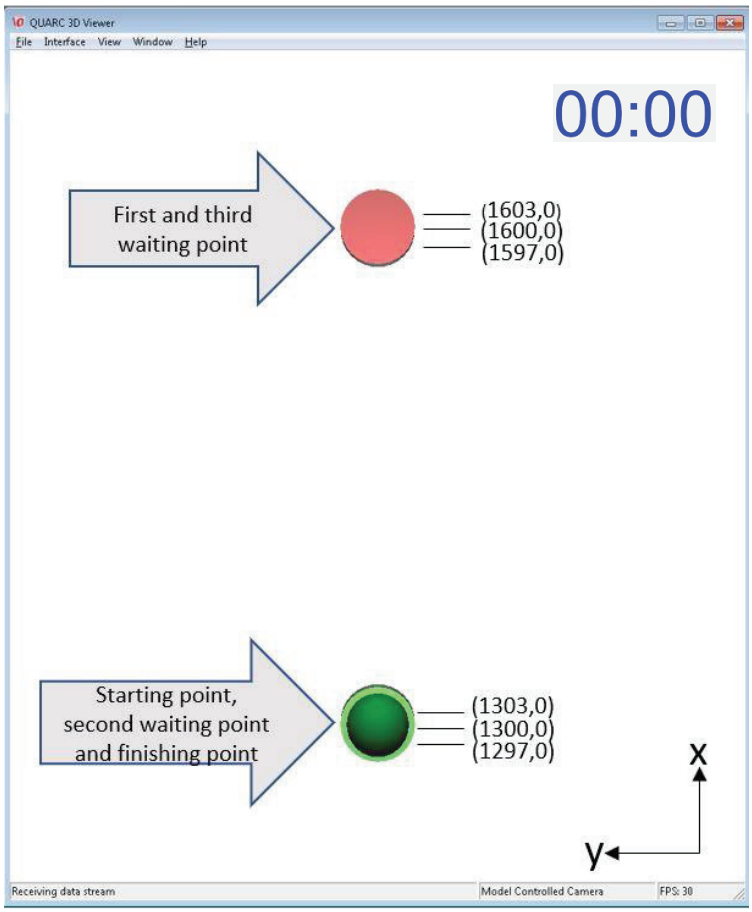

Figure 5.18. Graphical user interface

As the subject moves the robot end-effector in the +x axis direction (as he pushes the handle), the sphere in GUI will move upwards, as the operator moves the robot end-

effector in the -x axis direction (as he pulls the handle), the sphere goes down on the screen. When the experiment starts, subject is demanded to move the robot end-effector on the +x axis to move the sphere up and stop at the intended place, which is identified with a pink circle, and wait for 4 s. After that, the subject moves the sphere down and stops at the new target identified by the pink circle, which is the initial position of the sphere, and wait for 4 s. The subject repeats this sequence of motion once more to complete the test. Accordingly, each subject waits for 4 s for 3 times in total during the experiments. The subjects are asked to perform each movement within 6 s in one direction. In addition, the subjects are informed about the color of the targeted point. When the subject moves the sphere inside the target for the first time, the color of the target changes to green. This indicates that the 4 s count has begun. If the subject moves outside the target before 4 s has completed, the target changes its color to pink to indicate this event however, 4 s count still continues. The subject observes the time spent inside the target via a clock shown in Figure 5.18. The admittance terms in y and z directions are set to zero so that the subject can only make the robot move along the x direction. A total of 10 subjects are included in the study and each subject performs 8 experiments with different admittance parameters.

The distance between two points where the subjects wait in each direction is 300 mm. The subjects try to hold the robot's end-effector within a tolerance range of 6 mm. The admittance term parameters that are used in the experiments are given in the Table 5.1.

Table 5.1. Mass-damper parameters

Admittance Term Parameters			
Experiment Number	(m_x) Mass (kg)	(b_x) Damper (Ns/m)	(ω_{cx}) Corner Frequency (rad/s)
1	100	100	1
2	200	100	0,5
3	300	100	0,33
4	400	100	0,25
5	100	200	2
6	200	200	1
7	300	200	0,66
8	400	200	0,5

In the first four experiments (1 to 4) shown in the Table 5.1, the damper parameter is kept constant at 100 Ns/m while the mass parameter is changed by 100 kg in between each experiment. In the second four experiments (5 to 8), the damper term is increased to 200 Ns/m and the mass terms are increased in the same manner of the first four experiments. In addition, the corner frequency is the same in experiments 1 and 6, and experiments 2 and 8.

Before the experiments, the selected admittance term are validated. The reason for this is to check if the specified parameters are suitable to be used in the experiments and if the calculated parameters from the test results match the selected parameters. The procedure for this test is as follows. The velocity demand for the SHAD robot is generated by the ΔF_x input subjected to the selected admittance term with parameters $m_x = 400$ kg and $b_x = 200$ Ns/m. Since the desired force is set to zero for full backdrivability, ΔF input is the negative of the measured interaction force between the user and the handle. In this test the user followed the test procedure defined by using the GUI described previously. The velocity of the robot's end-effector along x direction, V_m, is acquired and then is used in Equation 5.11 to calculate the computed interaction forces, F_c.

$$F_{cx} = m_x \dot{V}_x + b_x V_x \tag{5.11}$$

F_{cx} and ΔF_x plots against time are given in Figure 5.19. The difference between the two plots are considerably small which indicates that the desired admittance parameters are actually implemented during the test and the user could complete the task with the selected range of admittance term parameters.

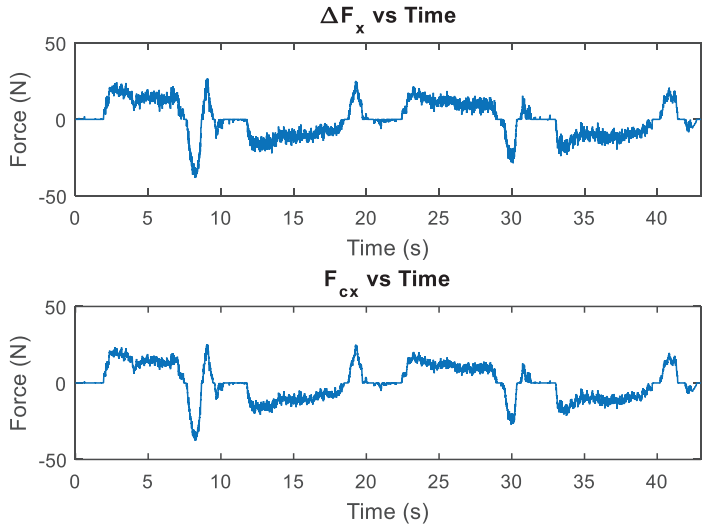

Figure 5.19. ΔF_x and F_{cx} comparison

The effect of the mass term on the accuracy is investigated by comparing the test results of the experiments 1 to 4 and 5 to 8 and the effect of the damper term on accuracy is investigated by comparing the test results of the experiments 1-5, 2-6, 3-7 and 4-8. Besides, while the corner frequency is the same, the effect of the change of mass and damper terms together is investigated by comparing the results of experiment 1-6 and experiment 2-8. To compare test results, the mean squared errors of the end-effector's position while the user tries to hold the end-effector at the exact target location for 4 s is used. The mean squared errors for each experiment and the average of mean squared errors are shown in Table 5.2. The graph of the average of the mean squared errors are also shown in Figure 5.20. It should be noted that, mean squared error is calculated according to 1600 mm at the first and third waiting points, and according to 1300 mm at the second waiting point.

Table 5.2. Mean squared errors of all experiments

Mean Squared Error (mm^2)											
Sub. # / Exp. #	1	2	3	4	5	6	7	8	9	10	Average
1	17,03	8,36	2,95	4,50	3,10	5,14	17,22	12,56	7,33	27,38	10,56
2	9,77	16,54	18,67	15,53	8,55	14,22	34,13	21,27	16,26	28,34	18,33
3	29,06	19,31	37,22	5,37	19,30	16,61	17,32	14,32	24,54	6,12	18,92
4	35,71	62,90	100,60	69,95	20,50	96,90	41,71	13,38	144,00	16,00	60,16
5	12,78	8,46	11,85	5,89	1,35	15,91	3,34	18,93	7,02	6,06	9,16
6	17,36	2,51	5,43	8,45	9,67	20,44	17,04	3,37	8,22	6,22	9,87
7	6,44	5,44	15,87	13,59	11,45	9,34	30,70	11,14	14,96	2,26	12,12
8	23,29	41,85	29,59	11,48	9,78	11,05	27,99	15,23	18,93	10,27	19,95

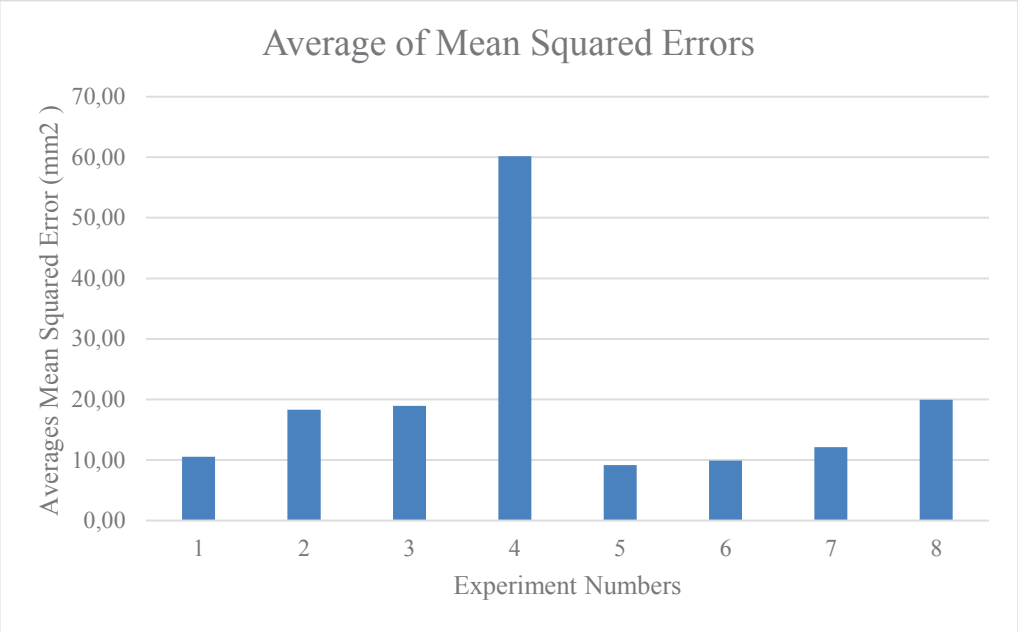

Figure 5.20. Average of the mean squared errors of the experiments

When the first group of four experiments is investigated, the mean squared errors increase from experiment 1 to experiment 4, and experiment 4 has a considerably higher error with respect to the other ones. When the second group of four experiments is investigated, the mean squared errors increase from experiment 5 to experiment 8, and experiment 8 has a considerably higher error with respect to the other ones. These results indicate that when the damper term is kept constant and the mass is increased, the accuracy decreases. Experiments 1-5, 2-6, 3-7, and 4-8 are the experiments in which mass term is kept constant and the damper term is changed relatively. When these experiment results are investigated according to mean squared errors, it is observed that when the mass is kept constant, damper term is increases, the mean squared error is decreases indicating that the accuracy increases. Experiments 1-6 and 2-8 are the experiments that have the same corner frequency. When the results of these experiments are investigated according to mean squared errors, it is observed that, when the corner frequency is kept constant even if the mass term and damper term are different, the accuracy level is almost the same.

Table 5.3. Sum of applied forces by the subjects during experiments

Total Applied Force (N)								
Exp. # / Sub. #	1	2	3	4	5	6	7	8
1	159,50	212,01	263,00	345,08	274,26	283,83	295,13	406,21
2	128,61	181,51	207,49	312,47	247,66	263,82	298,09	355,00
3	134,32	187,97	277,14	288,04	258,65	293,27	333,49	387,99
4	148,17	178,03	212,78	304,29	265,67	273,11	335,48	346,95
5	135,87	172,41	254,00	247,02	242,38	273,49	295,72	378,33
6	130,82	167,78	234,14	289,73	244,01	258,80	282,81	343,56
7	154,18	206,91	269,52	332,95	244,34	314,73	373,46	423,38
8	130,93	181,35	266,96	245,35	250,95	254,09	316,77	398,85
9	139,55	166,35	279,57	308,19	253,80	270,06	316,32	374,02
10	138,44	209,14	231,30	236,51	253,27	257,17	282,83	334,88
Average	140,04	186,34	249,59	290,96	253,50	274,24	313,01	374,92

Table 5.3 shows the sum of applied force by the subjects during experiments and Figure 5.211 shows average of the sum of forces measured for the use of each admittance term.

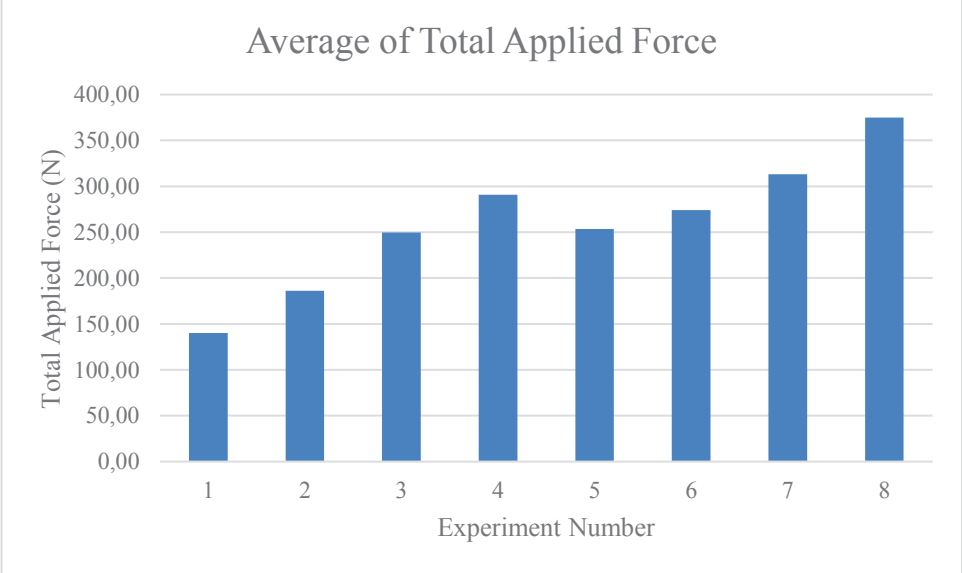

Figure 5.21. Average of total applied force

When the sum of applied forces is taken into account during the experiments, the sum of forces applied to the same task is increased when the damper term is kept constant and the mass term is increased (as experiments 1 to 4 and 5 to 8). In addition to this, when the mass term is kept constant and the damper term is increased (in experiments 1-5, 2-6, 3-7 and 4-8), the sum of forces required to do the same task increases. Experiments 1-6 and 2-8 are the experiments that have same corner frequency. From these experiments, it is observed that, when the mass terms and damper terms are increased together but the corner frequency is kept constant, the total force applied to the same task increases.

How well the subject holds the end-effector stationary at the targeted locations is evaluated by investigating the standard deviation of the position of the end-effector during the 4 s the subjects hold the robot's end-effector at the targeted locations. The effect of the mass term on this criterion is investigated by comparing the test results of the experiments 1 to 4, and 5 to 8. The effect of the damper term on this criterion is investigated by comparing the test results of the experiments 1-5, 2-6, 3-7, and 4-8. The results of the experiments in terms standard deviations and average of the standard deviations are given in Table 5.4. The graph of the average of the standard deviations is also shown in Figure 5.222.

Table 5.4. Standard Deviations of All Experiments

Standard Deviations (mm)											
Sub. # / Exp. #	1	2	3	4	5	6	7	8	9	10	Average
1	2,50	0,95	0,81	1,14	1,02	0,98	1,26	1,14	1,21	2,24	1,32
2	1,92	1,04	2,34	1,52	1,55	1,81	3,42	2,56	1,97	1,78	1,99
3	3,08	1,61	4,27	1,33	2,85	1,68	2,44	1,80	3,53	1,41	2,40
4	2,62	3,51	6,02	3,71	2,42	6,99	2,86	2,07	7,36	2,41	4,00
5	2,29	0,88	1,77	0,94	0,70	1,30	0,80	1,27	1,53	1,28	1,28
6	1,40	0,90	1,37	1,38	1,13	1,71	1,93	1,05	1,59	1,10	1,35
7	1,17	0,86	2,45	1,88	1,06	1,15	2,04	1,71	2,25	0,91	1,55
8	2,89	3,42	3,15	1,67	2,04	1,71	3,29	1,59	1,95	1,84	2,36

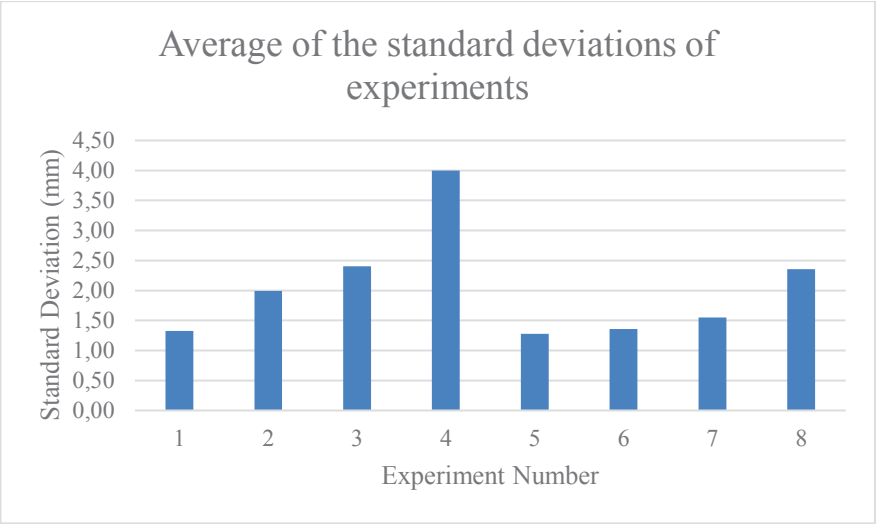

Figure 5.22. Average of the standard deviations of the experiments

When the first group of four experiments is investigated, the standard deviations increase from experiment 1 to experiment 4, and experiment 4 has a considerably higher standard deviation with respect to the other ones. When the second group of four experiments is investigated, the standard deviations increase from experiment 5 to experiment 8, and experiment 8 has a considerably higher standard deviation with respect to the other ones. According to these investigations, when the damper term is kept constant and the mass is increased, the standard deviation increases, and therefore the ability of the subject holding the end-effector at a stationary location is adversely affected. Experiments 1-5, 2-6, 3-7, and 4-8 are the experiments that the mass term is kept constant and the damper term is changed. When these experiment results are investigated according to their standard deviations, it is observed that when the mass is kept constant and damper term is increased, the standard deviation decreases, and therefore, the ability of the subject holding the end-effector at a stationary location is positively affected. Based on these test results, it is not possible to pass a judgement on change in the ability of the subject holding the end-effector at a stationary location when different admittance parameters are used resulting in the same corner frequency.

CHAPTER 6

CONCLUSION

In this thesis, a compliance controller along with obstacle avoidance subtask is proposed for and implemented on SHAD redundant robot. SHAD is a 4 DoF robot which is kinematically redundant with respect to the three-dimensional positioning tasks. A force sensor is attached to its distal end, end-effector, which enables a human operator to control the SHAD by applying force through the handle mounted on the end-effector. A compliance controller, namely admittance controller, is utilized for SHAD's control scheme to regulate the motion of the robot with respect to the induced forces on the handle by the human operator. Since SHAD is designated to be used by a human operator, who is located inside the robots workspace, in direct physical interaction, there is a possibility that the SHAD robot's links might collide with the operator. For safer operations, an obstacle avoidance algorithm is devised to avoid possible collisions with human operator. Obstacle avoidance algorithm regulates the motion of each link of the SHAD robot with respect to their distance to the obstacle (in this case, the human operator) while the end-effector motion is not disturbed thanks to the robot's kinematic redundancy. Obstacle avoidance algorithm is applied making use of null space of the Jacobian matrix with pseudo inverse approach.

The controller developed for obstacle avoidance is verified in simulation environment and later tested in the experimental setup. After the experimental tests with obstacle avoidance are concluded and it is verified that the robot's link can be moved away from a human operator located inside the robot's workspace, admittance control experiments are initiated. In admittance control experiments, the effects of parameters in admittance terms are investigated according to accuracy, sum of applied forces by the user which indicates the total effort by the user, and ability to hold end-effector at a stationary location. To investigate effects mass term, mass term is changed while the damper term is kept constant. The damper term's effect is examined by changing damper term while mass term is kept constant. Experiments are executed with 10 subjects and 8 experiments are executed per subject. The experiment results show that, the increase in the damper term increases the accuracy, the total applied force and the ability to hold the

end-effector at a stationary location. The increase in the mass term decreases the accuracy, increases the total applied force and decreases the ability to hold the end-effector at a stationary location. Additionally, when the admittance terms are designed to have the same corner frequency with different parameters, they result in the same accuracy levels however, the total effort by the user increases as the parameters are increased.

SHAD system has considerably large joint clearances and as a future study, input shaping method can be implemented for reducing residual vibrations on the system due to these joint clearances. Since SHAD system is currently used as an admittance type haptic device, minimum and maximum impedance and transparency of the device can be measured as future studies to be conducted on SHAD system.

REFERENCES

Adams, R.J., & Hannaford, B. (2002). "Control Law Design For Haptic Interfaces To Virtual Reality". *IEEE Transactions On Control Systems Technology* 10 (1): 3-13. doi:10.1109/87.974333.

Ahmed, R.M. (2011). *Compliance Control Of Robot Manipulator For Safe Physical Human Robot Interaction*. Örebro: Örebro University.

Anderson, R.J., & Spong, M.W. (1988). "Hybrid Impedance Control Of Robotic Manipulators". *IEEE Journal On Robotics And Automation* 4 (5): 549-556.

Argyros, A. A., Bekris, K.E., & Orphanousdakis, S.C. (2001). Robot Homing based on Corner Tracking in a Sequence of Panoramic Images. *In Proc. Of CVPR'01*. Hawaii. Usa.

Bilgincan, T., Gezgin, E., & Dede, M. I. C. (2010). *Integration of the Hybrid-Structure Haptic Interface HIPHAD v1.0.* Proceedings of the International Symposium of Mechanism and Machine Theory. October 5-8. Izmir.

Colgate, J. E. & Brown J.M. (1994). *Factors Affecting the Z-Width of a Haptic Display*. *Robotics and Automation.* 3205- 3210.

Conkur, E.S. & Buckingham R. (1997). *Clarifying the Definition of Redundancy As Used in Robotics*. *Robotica*. 15(5). 583–586.

Dede, M.İ.C. (2003). *Position/force Control of Robot Manipulators.* Master's thesis, Middle East Technical University.

Dietrich, F., Kaiser, K., Ellwood, R.J., & Raatz A. (2010). "An Autonomous and Safe Homing Strategy for Parallel Kinematic Five-Bar Manipulators." *Advances in Robot Kinematics: Motion in Man and Machine*, 501-08.

Fodor, G., & Tevesz, G. (1999).Hybrid Position and Force Control Algorithm Expansion of a Robot Control System, *Periodica Polytechnica Ser. El. Eng*., 43(4), 251-261.

Hertenstein, M., & Weiss, S.J. (2011). *The Handbook of Touch: Neuroscience, Behavioral, and Health Perspectives.* Springer Publishing Company.

Hirche, S., & Buss, M. (2012). *Human-oriented Control for Haptic Teleoperation*. *Proceedings of the IEEE*, 100(3), 623-647.

Işıtman, O. (2018). *Compliant Control of a Teleoperated Endoscope Robot*. Master's Thesis, Izmir Institute of Technology, Izmir, Turkey.

Jin, M., Kang, S.H., & Chang P.H. (2008). *Robust Compliant Motion Control of Robot with Nonlinear Friction Using Time-Delay Estimation*. IEEE Transactions on Industrial Electronics. 55(1). 258 – 269.

Kanık, M., Berker, G., Maaroof, O., Uzunoğlu, E., & Dede, M.İ.C. (2017). *Admitans Yapısında Kinematik Olarak Artıksıl Haptik Ana Sistem Tasarımı*. 18. Ulusal Makina Teorisi Sempozyumu. 5-7 Temmuz. Trabzon.

Kern, T. A. (2009). *Engineering haptic devices: a beginner's guide for engineers*. Springer Science & Business Media.

Khosla P. and T. Kanade. (1989). *Real-time Implementation of The Computed Torque Scheme*. *IEEE Transactions on Robotics Automation*. 5(2). 245–253.

Koul, M. H., Manivannan, M., & Saha, S. K. (2013). *Enhancing the Z-width of Haptics Interfaces through Dual-rate Sampling*. In Proceedings of Conference on Advances In Robotics (1-6). ACM.

Lawrence. D. A. (1993). *Stability and Transparency in Bilateral Teleoperation*. *IEEE Transactions on Robotics and Automation.* 9(5). 624-637.

Lee, D. Y., Nam, Y. J., Park, M. K., & Yamane, R. (2010). *Transparency improvement of a 1 DOF hybrid haptic device with wide-ranged torque reflection*. *International Journal of Applied Electromagnetics and Mechanics*, 33 (1, 2).

Lee, K.K., & Buss, M. (2007). *Obstacle Avoidance for Redundant Robots Using Jacobian Transpose Method.* Intelligent Robots and Systems International Conference. San Diego. USA.

Maaroof, O. (2012). *Self – Motion Control of Kinematically Redundant Robot Manupilators* (Master's thesis). A Thesis Submitted To The Graduate School Of Engineering and Sciences Of The İzmir Institute of Technology.

Maciejewski, A.A., & Klein, C.A. (1985). *Obstacle Avoidance for Kinematically Redundant Manipulators in Dynamically Varying Environments*. *The International Journal of Robotics Research.* 4(3). 109 – 117.

Madani, T., Daachi, B., & Benallegue, A. (2013). *Adaptive Variable Structure Controller of Redundant Robots with Mobile/Fixed Obstacles Avoidance*. *Robotics and Autonomous Systems.* 61(6). 555 – 564.

Ott, C., Mukherjee R., & Nakamura, Y. (2010). *Unified Impedance and Admittance Control*. 2010 IEEE International Conference on Robotics and Automation. 3-7 May 2010. Anchorage, Alaska, USA.

Peer, A., & Buss M. (2008). *A New Admittance-Type Haptic Interface for Bimanual Manipulations*. *IEEE/ASME Transaction and Mechatronics.* 416 – 428.

Schutter, J. D., & Brussel. V.H. (1988). *Compliant Robot Motion II. A Control Approach Based on External Control Loops*. *The International Journal of Robotics Research.* 7(4). 18-33.

Seraji, H. (1991). *Task Options for Redundancy Resolution Using Configuration Control*, IEEE Conf. on Decision and Control, Brighton, England. 3. 2793-2798.

Seraji, H. (1994). *Adaptive Admittance Control: An Approach to Explicit Force Control in Compliant Motion*. *Robotics and Automation.*

Siciliano, B., & Oussama, K. (2008). *Handbook of Robotics*. Springer.

T. Yoshikawa. (1984). *Analysis and control of robot manipulators with redundancy*. *Robotics Research The First International Symposium*. MIT Press.735-747.

Tatematsu, A., & Ishibashi, Y. (2010). *Mapping Workspaces to Virtual Space in Work Using Heterogeneous Haptic Interface Devices*. IntechOpen.

Tatlicioglu, E., McIntyre, M.L., Dawson, D.M., & Walker, I.D. (2005). *Adaptive Nonlinear Tracking Control of Kinematically Redundant Robot Manipulators with Sub-task Extensions*. Proceedings of the 44th IEEE Conference on Decision and Control Seville, Spain.

Van der Linde, R. Q., Lammertse, P., Frederiksen, E., & Ruiter, B. (2002). *The HapticMaster, A New High-performance Haptic Interface.* Paper presented at the Proc. Eurohaptics.

Varalakshmi, B. D., Thriveni, J., Venugopal, K. R., & Patnaik, L. M. (2012). *Haptics: State of the Art Survey*. International Journal of Computer Science Issues, 9(5).

Volpe, R. & Khosla, P. (1995). *On The Equivalence of Second Order Impedance Control and Proportional Gain Explicit Force Control*, *The International Journal of Robotic Research.* 14(6). 574-589.

Vukobratovic, M., Surdilovic, D., Ekalo, Y., & Katic, D. (2007). *Dynamics and Robust Control of Robot-Environment Interaction*. *New Frontiers in Robotics*. 2.

Whitney, D. (1985). *Historical Perspective and State of The Art in Robot Force Control*. In 1985 *IEEE International Conference on Robotics and Automation Proceedings*. 2. 262–268.

Yu, W., Rosen, J., & Li, X. (2011). *PID Admittance Control for an Upper Limb Exoskeleton.* American Control Conference.

Zeng, G. & Hemami, A. (1997). *An Overview of Robot Force Control*, *Robotica*, 15. 473-482.

Zlajpah, L., & Nemec, B. (2002). *Kinematic Control Algorithms for On-Line Obstacle Avoidance for Redundant Manipulators.* Intelligent Robots and Systems International Conference. 30 Sept – 04 Oct. Lausanne. Switzerland.

APPENDIX A

CONTROL PANEL CONNECTIONS

Connections must be made to drive the motors. This section describes the wiring of these connections. Figure A.1 shows the control panel. The control panel consists of five drives and six electrical terminals. The electrical terminals are used to transmit signals between the DAQ and the drives.

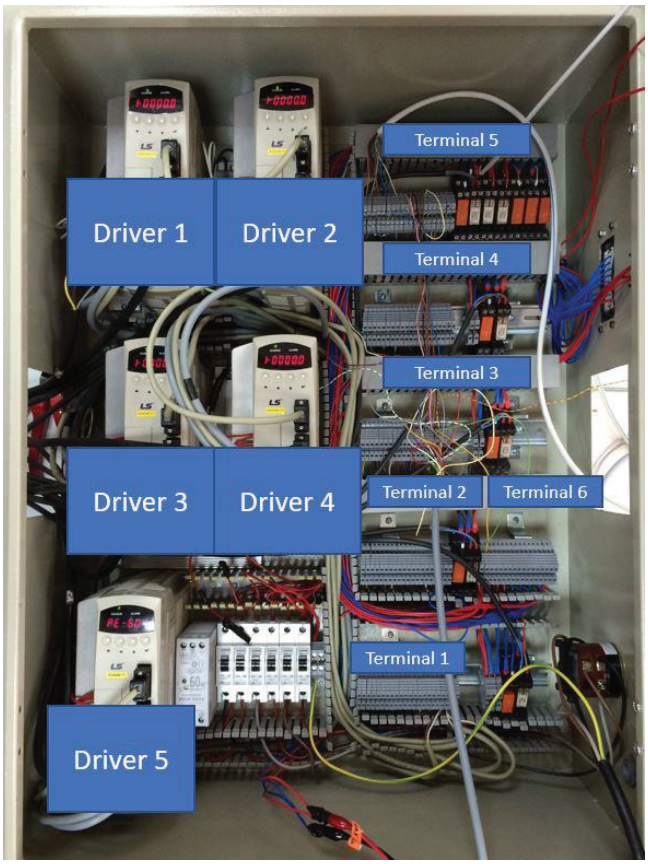

Figure A.1. Control Panel

In this thesis, four DoF mechanism is driven by using 1st, 2nd, 3rd, 4th drivers and their terminals Terminal 1, terminal 2, terminal 3, and terminal 4. The connections of the electrical terminals are given in Table A.1.

Table A.1 Electrical terminal connections

Electrical Terminal	Pin Number	Description	
Terminal 1,2,3,4	1	AO	Encoder Output
Terminal 1,2,3,4	2	/AO	Encoder Output
Terminal 1,2,3,4	3	BO	Encoder Output
Terminal 1,2,3,4	4	/BO	Encoder Output
Terminal 1,2,3,4	5	ZO	Encoder Output
Terminal 1,2,3,4	6	/ZO	Encoder Output
Terminal 1,2,3,4	7	OPC ZO	Encoder Output
Terminal 1,2,3,4	8	GND	Encoder Output
Terminal 1,2,3,4	9	SPDLMT	Analog Output
Terminal 1,2,3,4	10	TRQLMT	Analog Output
Terminal 1,2,3,4	11	GND	Analog Output
Terminal 1,2,3,4	12	MON1	Analog Input
Terminal 1,2,3,4	13	MON2	Analog Input
Terminal 1,2,3,4	14	GND	Analog Input
Terminal 1,2,3,4	15	PF+	For Position Operation Mode
Terminal 1,2,3,4	16	PF-	
Terminal 1,2,3,4	17	PR+	
Terminal 1,2,3,4	18	PR-	
Terminal 1,2,3,4	19	SVON	Servo On
K9, K10, K11, K12	14	Brake +	Brake Connection
K9, K10, K11, K12	24	Brake -	Brake Connection

The pins from the first pin to the eighth pin are used for encoder outputs. The pins from the ninth pin to the eleventh pin are used for analog outputs and these are speed and torque outputs. Twelfth, thirteenth, fourteenth pins are used for analog inputs. In addition, connections between the fifteenth and the eighteenth pins are used for position mode. Nineteenth pin is used for servo on.

APPENDIX B

ATI NANO 25 FORCE TORQUE SENSOR

In this thesis, ATI Nano 25 is used to perform force measurements. Figure B.1 shows ATI Nano 25 and Figure B.2 shows controller of force sensor.

Figure B.1. ATI Nano 25

The specifications of ATI Nona 25 Force / Torque sensor are given in Figure B.2.

Single-Axis Overload	
Fxy	±2300 N
Fz	±7300 N
Txy	±43 Nm
Tz	±63 Nm
Stiffness (Calculated)	
X-axis & Y-axis forces (Kx, Ky)	5.3×10^7 N/m
Z-axis force (Kz)	1.1×10^8 N/m
X-axis & Y-axis torque (Ktx, Kty)	6.5×10^3 Nm/rad
Z-axis torque (Ktz)	9.2×10^3 Nm/rad
Resonant Frequency	
Fx, Fy, Tz	3600 Hz
Fz, Tx, Ty	3800 Hz
Physical Specifications	
Weight*	0.0634 kg
Diameter*	25 mm
Height*	21.6 mm

** Specifications include standard interface plates.*

Figure B.2. Specification of ATI Nano 25